Article

Composite Materials with Nanoscale Multilayer Architecture Based on Cathodic-Arc Evaporated WN/NbN Coatings

Kateryna Smyrnova,* Martin Sahul, Marián Haršáni, Vyacheslav Beresnev, Martin Truchlý,
L'ubomír Čaplovič, Mária Čaplovičová, Martin Kusý, Andrii Kozak, Dominik Flock, Alexey Kassymbaev,
and Alexander Pogrebnjak

Read Online

ACCESS | 📊 Metrics & More | 📖 Article Recommendations

ABSTRACT: Hard nitride coatings are commonly employed to protect components subjected to friction, whereby such coatings should possess excellent tribomechanical properties in order to endure high stresses and temperatures. In this study, WN/NbN coatings are synthesized by using the cathodic-arc evaporation (CA-PVD) technique at various negative bias voltages in the 50−200 V range. The phase composition, microstructural features, and tribomechanical properties of the multilayers are comprehensively studied. Fabricated coatings have a complex structure of three nanocrystalline phases: β-W$_2$N, δ-NbN, and ε-NbN. They demonstrate a tendency for (111)-oriented grains to overgrow (200)-oriented grains with increasing coating thickness. All of the data show that a decrease in the fraction of ε-NbN phase and formation of the (111)-textured grains positively impact mechanical properties and wear behavior. Investigation of the room-temperature tribological properties reveals that with an increase in bias voltage from −50 to −200 V, the wear mechanisms change as follows: oxidative → fatigue and oxidative → adhesive and oxidative. Furthermore, WN/NbN coatings demonstrate a high hardness of 33.6−36.6 GPa and a low specific wear rate of $(1.9−4.1) \times 10^{-6}$ mm^3/Nm. These results indicate that synthesized multilayers hold promise for tribological applications as wear-resistant coatings.
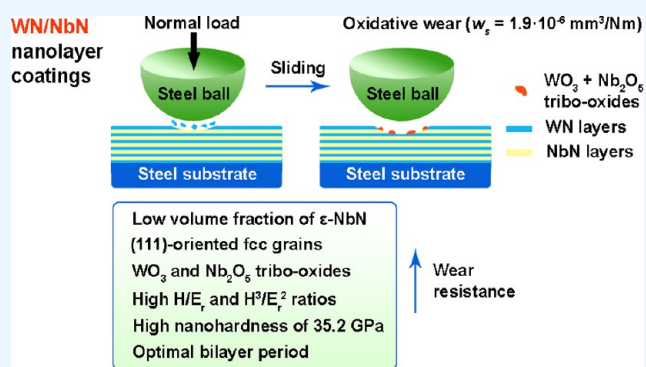
1. INTRODUCTION

Protective hard coatings have been widely used in the manufacturing industry since the late 1970s.[1] They find widespread application in various industries, serving as cutting tools for machining expensive and difficult-to-cut materials, as well as being utilized in manufacturing wind turbine blades, electronic devices, and aircraft and automotive components.[2] Yet they are most commonly used to protect the surfaces of cutting tools and components that operate under friction conditions. Typically, these coatings are synthesized by various physical vapor deposition (PVD) techniques, such as magnetron sputtering (MS), cathodic-arc evaporation, and ion-beam-assisted deposition.[3,4] They are characterized by generating the vapor phase from the solid phase (cathode material) by physical methods, followed by its transfer to a low-pressure region and its condensation on the substrate.[5,6] PVD methods can produce a wide range of dense coatings, including metastable ones, due to the high ionization of the reactant species bombarding the substrate and the ability to use low deposition temperatures and various reactive gases.[7,8] TiN was the first nitride coating for various cutting and forming tools that was produced by vaporizing solid titanium in a nitrogen

atmosphere.[9] This was followed by a rapid progression in the development of new protective coatings, such as TiAlN, TiSiN, ZrN, CrN, CrAlN, AlCrSiN, and TiCrAlSiN.[10−12] Despite the good functional properties of monolithic coatings, the multilayer design has proven its superiority. The alternating deposition of different materials enables the effective tuning of desired coating properties, including hardness, elasticity, wear resistance, fracture toughness, etc.[13−16]

Among the variety of multilayer transition metal nitride protective coatings, TiN- and CrN-based ones are the most studied due to their high hardness and wear resistance. For instance, TiN/CrN coatings showed a hardness of about 29.4 GPa and better oxidation and sliding wear resistance than monolithic CrN and TiN.[17,18] Huang et al.[19] reported that TiN/TaN multilayers exhibited an enhanced hardness of 36 ±

Table 1. Summary of Some Deposition Methods, Bilayer Period, and Mechanical and Tribological Properties of Reported WN-Based Multilayer Coating[a,b]

system	deposition method	bilayer period, Λ (nm)	hardness, H (GPa)	elastic modulus, E_r (GPa)	H/E_r	H^3/E_r^2 (GPa)	COF	wear rate, w_s (mm³/Nm)	ref
WN/ZrN	RF MS	30	34	423.8	0.08	0.219	0.76	3.8×10^{-4}	34
	CA-PVD	20	37.3	438.8	0.085	0.289	0.47	8.6×10^{-6}	30
WN/MoN	CA-PVD	15.3	35.5	419.7	0.085	0.254			30
WN/CrN	dual gun MS	24	30.5	199.9	0.152	0.71	0.31		35,36
	ion-beam-assisted deposition	30	26.3	247	0.106	0.298	0.315	3.8×10^{-6}	37
	MS	15	29.2	376	0.071	0.146	0.52	1.1×10^{-5}	38
	CA-PVD	14.5	33.3	393.4	0.085	0.239			30
WN/NbN	DC MS	7.4	43.7						33
	CA-PVD	21.1	35.7	383.9	0.093	0.309	0.55	1.7×10^{-6}	30
WN/TiN	DC MS	267	50.4	768.9	0.066	0.217	0.4	7.0×10^{-7}	39
	MS	2	28.1				0.55	2.0×10^{-6}	40
	DC (TiN) + pulsed DC (WN) MS	4	33.5	308.6	0.108	0.395	0.5		41
	DC MS	10.2	36.7	439	0.083	0.256			42
	DC MS	12	~36.0	236					43
	DC MS	81.2	28.5	328	0.087	0.215			44
WN/TiSiN	DC MS	81.2	28.5	328	0.087	0.215			44
WN/TiAlN	DC MS (WN) + multiarc ion plating (TiAlN)	373	~17.20				0.73	2.5×10^{-6}	45
WN/CrAlSiN	DC MS	20	30.7				0.23	1.02×10^{-6}	46
WN/TiAgN	DC MS	8	40.3	372.0	0.108	0.473	0.6		47,48
	MS	2	27.6	325	0.085	0.165	0.35	4.4×10^{-6}	49,50
WN/ (TiZrNbHfTa)N	CA-PVD	33	34	325	0.104	0.372			51

[a]RF MS—radio frequency magnetron sputtering. [b]DC MS—direct current magnetron sputtering.
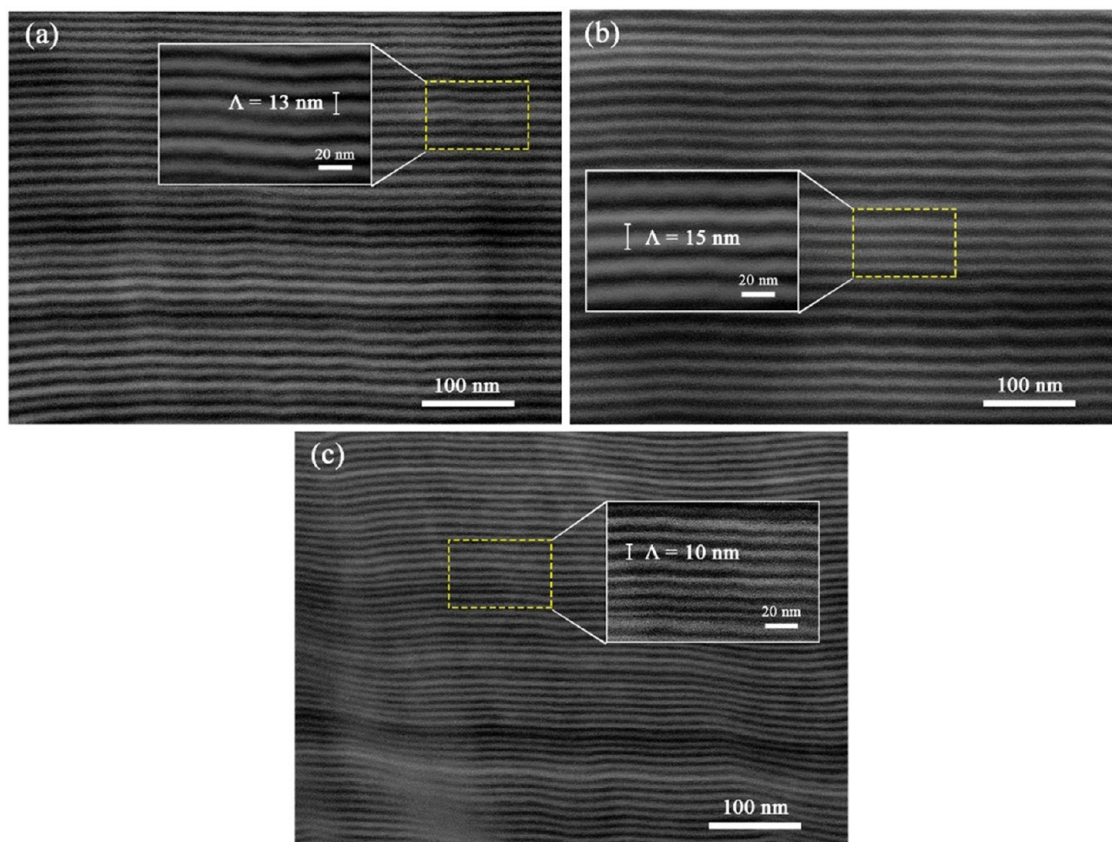
Figure 1. SEM cross-sectional micrographs of WN/NbN coatings deposited at different bias voltages: (a) −50, (b) −100, and (c) − 200 V.

2.4 GPa at the bilayer period (Λ) of 20 nm as a result of high stacking fault density. Combining TiN with MoN_y in the superlattice multilayer thin films resulted in critical fracture toughness and hardness of 4.1 ± 0.2 MPa $\sqrt{m}$ and 34.8 ± 1.6 GPa, respectively, which were superior to TiN.[20] In addition, CrN-based multilayer coatings are widely utilized in tribological applications. CrN provides a low coefficient of friction (COF) and good oxidation resistance due to the formation of a protective Cr_2O_3 layer.[13] For example, CrN/NbN multilayer coatings, forming oxides of Cr and Nb, demonstrated high resistance against water droplet erosion, tensile strength, and creep properties.[21] Moreover, CrN/MoN films showed hardness and wear rate up to 42.3 GPa and 5.92×10^{-7} mm^3/Nm, respectively, making them promising candidates for industrial applications.[22]

However, over the past decades, in addition to well-studied TiN and CrN coatings, WN has also captured the interest of scientists, fueling research and exploration across various scientific domains. Tungsten nitride can exist in two phases: fcc W_2N and hexagonal WN. Specifically, cubic W_2N has demonstrated the most distinctive and promising properties. For instance, W_2N films deposited using radio frequency reactive magnetron sputtering were stable at temperatures <800 °C with a hardness of 21.73 GPa.[23] Ghantasala and Sharma[24] reported that cubic tungsten nitride films exhibited self-lubrication properties, hardness of 28.36 ± 2.57 GPa, and low coefficient of friction of 0.303. At elevated temperatures (>150 °C), WN_x coatings form lubricating WO_3, decreasing COF.[25] Hence, W_2N is characterized by high thermal stability,[26] hardness,[27] adhesion strength to steel substrates,[25] wear resistance,[28] and specific capacity.[29] Such a diverse range

of properties open up numerous applications and stimulate new research into WN-based multilayer coatings. For instance, Table 1 summarizes the deposition parameters and mechanical and tribological properties of all WN-based multilayers designed up to the present date. It can be seen that the observed diversity among systems appears limited. The most significant number of articles have been published on multilayer coatings in which tungsten nitride was combined with well-studied titanium and chromium nitrides. However, beyond these two binary nitrides, WN-based multilayer systems have not yet been explored much. A few nanoscale multilayers incorporating ZrN, NbN, CrAlSiN, and (TiZrNbHfTa)N have also been reported. All existing research data demonstrate that WN-based multilayer coatings possess hardness greater than 26.3 GPa (only WN/TiAlN showed the lower value of 17.20 GPa), a low friction coefficient of 0.23–0.76, and a wear rate within the range of 7×10^{-7}–4.4×10^{-6} mm^3/Nm. However, although the exhibited properties suggest the potential of WN-based multilayer coatings, there is no comprehensive investigation of their wear behavior. Thus, further extensive studies of their tribological properties are required.

Furthermore, as can be seen, magnetron sputtering is the predominant deposition technique. In our previous study, we successfully synthesized WN/ZrN, WN/CrN, WN/MoN, and WN/NbN coatings under the same deposition conditions using the CA-PVD method and comprehensively characterized them.[30] This approach aimed to elucidate the system that exhibited the best tribomechanical properties. Thus, the WN/NbN coating demonstrated superiority over the other studied multilayers (Table 1). In addition to the high tribomechanical

properties of tungsten nitride, this is also due to the chemical inertness, thermal stability, and high wear resistance of niobium nitride.[31] For example, NbN with a hardness of 23.74 ± 0.58 GPa exhibited ultralow COF of 0.058 and wear rate of 1.79×10^{-10} mm³/Nm in a three-phase contact medium (water, air, and NbN) due to the tribochemical reactions with the formation of Nb_2O_5 particles.[32] Moreover, another study of NbN films synthesized by arc ion plating also showed a low wear rate of about 3.0×10^{-8} mm³/Nm. Considering the characteristics of WN and NbN, multilayer coatings based on these nitrides should have excellent wear-resistant properties. The only paper on WN/NbN films deposited by magnetron sputtering was published by Wen et al.[33] At a bilayer period of 7.4 nm, multilayers demonstrated a hardness greater than 40 GPa, but other properties were not reported. Therefore, we elected to conduct a more in-depth analysis of changes in the microstructure and tribological behavior of WN/NbN coatings upon variations in the deposition parameters.

This study aims to investigate the effect of the negative bias voltage on the phase composition, texture, mechanical properties, and room-temperature tribological performance of CA-PVD WN/NbN coatings. Emphasis has been placed on studying the texture evolution in multilayers and understanding the relationship between wear behavior and microstructural features.

2. RESULTS AND DISCUSSION

2.1. Coating Morphology. Figure 1 shows cross-sectional scanning electron microscopy (SEM) images at higher and lower magnifications of M-50, M-100, and M-200 coatings. All multilayers demonstrate a dense, well-defined layered structure. Bright layers represented tungsten nitride, and dark layers were assigned to niobium nitride since the backscattered electron emission rate is higher for elements with higher atomic numbers. The bilayer period clearly varied depending on the applied substrate bias. Coating deposited at the highest U_s had the thinnest layers with Λ of about 10 nm, while the difference in the bilayer period between the M-50 and M-100 samples was not that dramatic. Thus, deposited coatings had a nanolayered structure with Λ values in the 10−15 nm range. Consequently, variations in total coating thicknesses were also observed, following the same trend as the bilayer period: 4.7, 5.0, and 3.5 μm for M-50, M-100, and M-200, respectively. Applying higher negative bias voltage increases the re-sputtering rate of adatoms caused by the bombardment ion flux effect.[52] The balance between the nucleation and re-sputtering processes determined the coating thickness.

Table 2 provides the results of the chemical composition analysis, as determined by the WDS method. N concentration ranged from 49.1 to 51.1 atom %, indicating the nitrogen stoichiometry in the deposited multilayers. Applying the highest U_s of −200 V led to an increase in W content up to

24 atom % with an associated decrease in Nb and N concentrations. Such a high bias voltage improves the energy transmission to the substrate. Thus, ions of the cathode materials with higher energies may cause significant intermixing between depositing nitride layers and the re-sputtering of niobium by heavier tungsten.

2.2. Phase Analysis. The GIXRD patterns of the M-50, M-100, and M-200 coatings obtained at different ω angles of the incident beam are depicted in Figure 2. All deposited nanolayers consisted of three phases: fcc β-W_2N (No. 225, $Fm\overline{3}m$, JCPDF 25-1257), fcc δ-NbN (No. 225, $Fm\overline{3}m$, JCPDS 38-1155), and hexagonal ε-NbN (No. 194, $P6_3/mmc$, JCPDS 89-4757). The diffraction maxima were assigned to the following planes: W_2N (111), W_2N (200), W_2N (220), and W_2N (311); δ-NbN (111), δ-NbN (200), δ-NbN (220), δ-NbN (311), and δ-NbN (222); ε-NbN (004) and ε-NbN (104). The values of the crystal lattice constants of all three phases in the deposited coatings tended to gradually decrease with an increased substrate bias voltage (Table 3). The lattice parameters of the hexagonal ε-NbN agreed well with the experimental and theoretical results by Terao[53] (a = 2.960 Å, c = 11.270 Å), Zou et al.[54] (a = 2.9599 Å, c = 11.2497 Å), and Ivashchenko et al. (a = 2.975 Å, c = 11.300 Å).[55] That could be associated with the formation of vacancies, intermixing between W- and Nb-based nitride layers, which could distort crystal lattices, and the presence of compressive residual stresses.[56] It can be seen that all coatings consisted of nanograins of similar sizes ranging from 2.8 to 4.3 nm.

Measuring diffraction patterns at various incident ω angles allowed us to study in more detail the phase composition of the deposited WN/NbN multilayers. Records obtained at selected angles ω could be associated with microstructural features at a certain coating thickness. For instance, GIXRD patterns obtained at ω = 0.5, 1, 4, 8, and 10° were assigned to approximately the following penetration depths: 0.127, 0.254, 1.016, 2.027, and 2.530 μm.

Analysis of the GIXRD patterns of WN/NbN multilayers revealed that applying a substrate bias voltage of −100 V did not change the microstructure from the top layers to half the thickness of the coating (total thickness ≈ 5 μm). The intensity of reflections from the hexagonal NbN phase in the M-100 coating remained unchanged regardless of the ω angle. Furthermore, the coating demonstrated a (111) + (200) preferred orientation over the studied thicknesses with only a slight decrease in (200) intensity. Diffraction peaks were shifted toward smaller 2θ angles, which could indicate the presence of compressive stresses.[41,57] This was confirmed by estimating residual stresses using the $\sin^2\psi$ method. The coating deposited at U_s = −100 V demonstrated compressive stresses with an absolute value of 4.65 ± 0.29 GPa (Table 3).

GIXRD spectra of the M-50 multilayer obtained at ω ranging from 4 to 10° were similar to M-100, characterized by the competitive growth of (111) and (200) planes. However, patterns collected from a depth of about 250 nm started to transform. The intensities of the (200), (220), and (311) peaks of the fcc phases and reflections from ε-NbN significantly decreased. Moreover, at a thickness of about 130 nm most grains in the M-50 coating had a (111) orientation. Such changes suggest a potential reduction in the density of defects and an enhancement of the crystalline properties of a multilayer. By acquiring a crystallographic texture, the coating attempts to minimize the total energy.[58] Among all deposited WN/NbN multilayers, the GIXRD peaks of M-50 were shifted
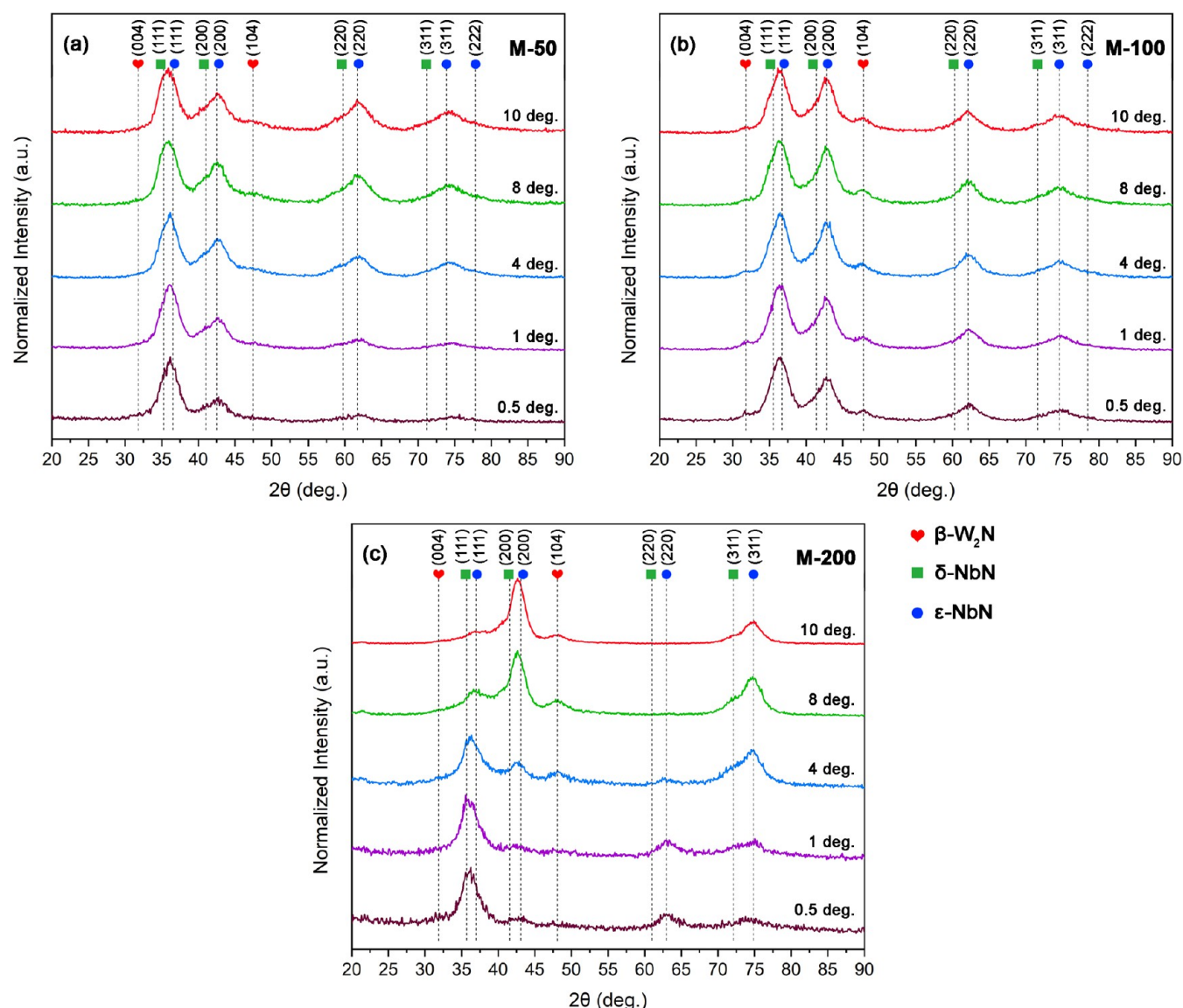
Table 2. Elemental Composition of the WN/NbN Coatings Deposited at Different Substrate Bias Voltages

coating	element concentration (atom %)		
	W	Nb	N
M-50	21.1	29.0	49.9
M-100	19.7	29.2	51.1
M-200	24.0	26.9	49.1

Figure 2. GIXRD patterns collected at ω angle from 0.5 to 10° of the nanolayered WN/NbN coatings deposited at various bias voltages: (a) −50 V, (b) −100 V, and (c) −200 V.

Table 3. Summary of Lattice Parameters, Grain Sizes, and Residual Stresses of WN/NbN Coatings Deposited at Different Negative Bias Voltages

	lattice parameter (Å)				grain size (nm)			
	ε-NbN		δ-NbN	β-W$_2$N				
coating	a	a	c	a	β-W$_2$N	ε-NbN	δ-NbN	residual stresses (GPa)
M-50	4.238	2.988	11.274	4.386	3.2	2.8	2.9	−6.93 ± 0.88
M-100	4.219	2.969	11.252	4.358	3.4	4.3	3.2	−4.65 ± 0.29
M-200	4.194	2.938	11.229	4.332	3.7	3.6	3.7	−2.78 ± 0.56

toward smaller angles the most because of the highest compressive residual stresses (−6.93 ± 0.88 GPa).

The M-200 multilayer showed a variation in crystallographic orientation throughout the coating. Since its total thickness is about 3.5 μm, the GIXRD pattern is shown at $\omega = 10°$. covers the structural features from almost the entire coating. Thus, the evolution of the crystalline grain orientation was abrupt as the coating thickness increased. The WN/NbN coating developed the (200) preferred orientation at the initial growth stage. The W$_2$N (220), δ-NbN (220), and δ-NbN (222) peaks were

missing, unlike other coatings. At a depth of about 2 μm from the surface, the intensity of the (111) and (311) planes of fcc phases increased. GIXRD pattern obtained at 1 μm from the surface ($\omega = 4°$) revealed that the (200) peaks continued to fade to the point that most grains were oriented within (111) and (311) directions. Finally, the structure of a coating area close to the surface (127−254 nm) was characterized by a strong (111) preferred orientation, which is the most close-packed plane. Moreover, the ε-NbN reflections were almost undetectable and (220) planes appeared. Similar behavior of
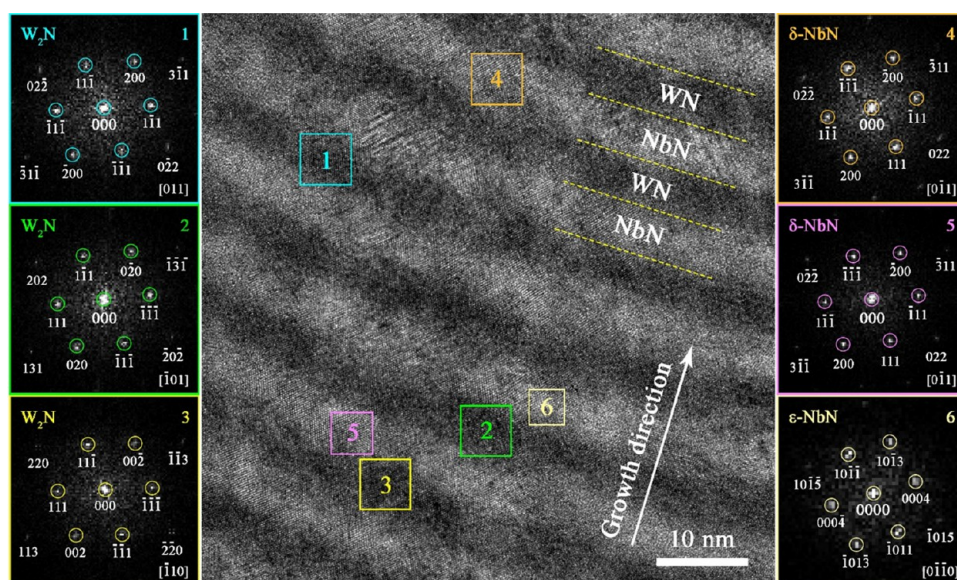
Figure 3. Cross-sectional bright-field TEM image with FFT patterns from selected regions of the WN/NbN coating deposited at U_s = −200 V.

the hexagonal NbN phase at the same ω angles was observed in the M-50 multilayer. That could mean that during deposition, at some critical thickness, the M-50 and M-200 coatings began to grow pseudoepitaxially at approximately the top 200 nm-thick layer.

The evolution of the preferred orientation of grains can occur during the nonequilibrium deposition process.[59,60] Although the texture depends on many factors, the main parameters include total coating thickness, bilayer period in multilayers, deposition temperature, substrate bias voltage, and the difference in thermal expansion coefficients of substrate and coating.[61,62] Among the deposited WN/NbN multilayers, the most drastic texture evolution from (200) to (111) was observed for the coating, with the lowest bilayer period of 10 nm deposited at the highest bias voltage. Less pronounced changes then characterized the M-50 multilayer with a little greater Λ of about 13 nm. Finally, the coating with Λ = 15 nm demonstrated only a slight decrease in the (200) plane intensity. It should, therefore, be noted that the tendency for (111)-oriented grains to overgrow (200)-oriented grains was inherent to all coatings to varying degrees.

The growth of grains is a complex process that is characterized by the competitive evolution of certain grains at the cost of others.[61] Different crystallographic orientations are favored by either surface and interface energy coatings or strain energy minimization.[63] Alterations in the texture of the WN/NbN coatings throughout the thickness can be explained by the anisotropies in the atomistic processes taking place on different surfaces. It has been shown that during grain formation and growth in nitride film deposited at a high bias voltage, the system tries to minimize the total surface and interface energy, which favors the (200)-oriented grains.[64,65] Therefore, at the early phase of the coating growth, the (200) surface is dominant as it provides a high diffusivity of adatoms. Further, as the thickness of the multilayer increases, low potential energy (111) surfaces slowly start to dominate. Thus, a texture evolution in the M-200 coating is controlled solely by kinetic effects.[66] However, at lower energies of bombarding ions (M-50 and M-100), the balance between kinetic factors and thermodynamically driven growth governs the formation

of a mixture of (111)- and (200)-oriented grains. When the low-diffusivity (111) surfaces slightly overgrow the (200) planes, kinetic effects come to the forefront. Moreover, the minimization of compressive residual stresses in nitride films may govern the growth of (111) surfaces responsible for strain minimization.[63]

In general, nitride coatings deposited by the CA-PVD method often have high compressive stresses, which positively affect tribomechanical properties.[1] A study of residual stresses of niobium nitride revealed higher compressive strains in films with a mixed (111) + (200) texture compared to a strong (111) preferred orientation.[66] In addition, the absolute value of compressive stresses was higher in the case of an increase in the $I_{(111)}/I_{(200)}$ ratio. We observed a similar behavior of WN/NbN coatings deposited at different bias voltages. The residual stresses in WN/NbN coatings deposited at absolute values of the negative bias voltage ranging from 50 to 200 V demonstrated a descending dependence (Table 3). The M-200 multilayer had the lowest compressive stress of 2.78 ± 0.56 GPa. High-energetic ion bombardment due to a high substrate bias voltage elevates the deposition temperature. This, in turn, significantly affects the adatom mobility and diffusivity. Therefore, atoms at the surface of the growing film can migrate to the grain boundaries and occupy more energetically favorable positions. Along with texture evolution, such a process promotes the release of residual stresses in the coating deposited at higher U_s values.[58,64,67]

2.3. Microstructural Characterization. The bright-field transmission electron microscopy (TEM) image of the M-200 cross section was reported in Figure 3. It was found that the WN layers had a slightly lower thickness than that of NbN due to the instabilities of an electric arc of the tungsten cathode. The average bilayer period was calculated to be approximately 10 nm, which agreed well with the SEM findings. The distinct feature of the nanolayer coating deposited at the highest bias voltage was blurred interfaces between the layers. Fast Fourier transform (FFT) patterns from various areas of the sample were obtained to determine the phase composition of each individual nitride layer. The analysis of WN layers represented by dark lines revealed only crystallites of the NaCl-type β-W_2N
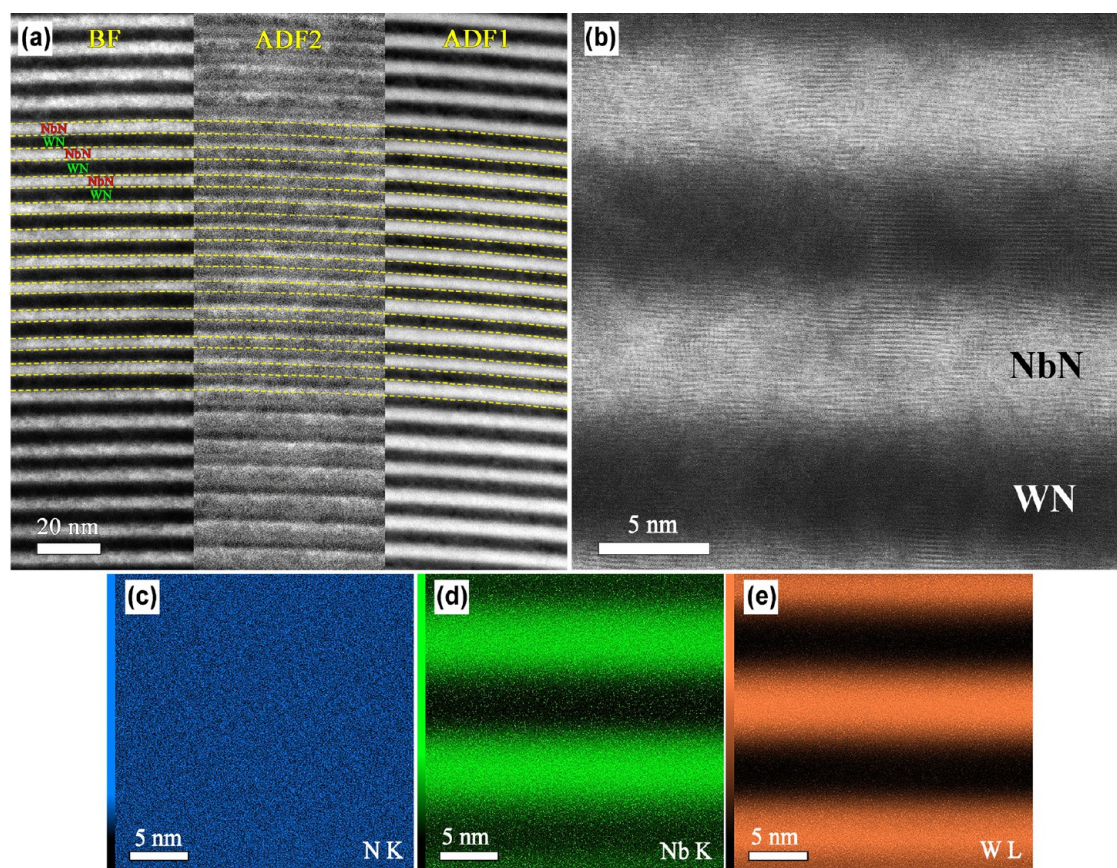
Figure 4. Combined STEM image of the WN/NbN coating deposited at a bias voltage of −200 V acquired simultaneously with BF, HAADF (ADF1), and LAADF (ADF2) detectors (a). A high-resolution STEM image in BF mode (b) and EDS elemental mapping images (c-e) of the M-200 multilayer.

in different parts of the coating. The crystallites were oriented within the <110> type zone axes. In contrast, the light layers ascribed to niobium nitride exhibited a more complex structure with nanocrystallites of the fcc δ-NbN and hexagonal ε-NbN phases. Similar to β-W$_2$N, cubic δ-NbN was oriented within the $[0\bar{1}1]$ direction of the <110> type. This type of crystallite orientation prevailed because of the lamella's chosen orientation. Therefore, the three phases β-W$_2$N, δ-NbN, and ε-NbN coexisted in the deposited nanolayer coatings, which was in good agreement with the X-ray diffraction data.

For a detailed characterization of the interface between deposited WN and NbN nanolayers, the M-200 coating was analyzed simultaneously using different scanning TEM (STEM) regimes (Figure 4a). In particular, bright-field, high-angle annular dark-field (ADF1), and low-angle annular dark-field (ADF2) detectors. The difference between ADF1 and ADF2 is the collection angles of scattered electrons. ADF1 geometry allows it to detect signal within 50−250 mrad, while inner-outer angles of the ADF2 detector signal correspond to 25−50 mrad.[68] Thus, a high-angle annular dark-field detector is sensitive to the atomic number Z and uses incoherently scattered electrons for imaging. Meanwhile, a low-angle annular dark-field signal is sensitive to strain fields from the defects that cause dechanneling of the incident electrons. The image in this mode is formed by collecting incoherently and coherently scattered electrons.[69] The BF image is created by a direct beam weakened due to the interaction with the coating being studied, making the crystalline areas appear dark.

The ADF1 part of the STEM image demonstrated an alternated stack of dark and bright layers ascribed to niobium nitride and tungsten nitride nanolayers, respectively. Moreover, the BF and ADF2 parts of Figure 4a provide a better understanding of the features of interlayer interfaces. It can be seen that no sharp boundaries were observed. This finding means that high-energy incident particles hitting the growing surface of the coating due to high bias voltage resulted in the intermixing between WN and NbN layers. Additionally, a low-angle annular dark-field part of the STEM image exhibited a positive contrast at the interlayer interfaces, appearing as bright regions. Such areas with increased intensity in the LAADF regime indicate the strained regions that cause changes in diffraction conditions.[70,71] Strain causes an intense signal due to the electron probe dechanneling.[72] Thus, intermixing between layers deposited at high U_s values created deformed regions with dislocations and high stresses. The BF high-resolution image of the coating cross section showing interfaces between different constituent nitride layers is reported in Figure 4b. Interfaces between layers were not sharp, and NbN layers had many distortion regions because of the complex structure composed of cubic and hexagonal phases. The lattice fringes also appear to be continuous between different nitride layers. In order to transmit the in-plane crystallographic orientation within the coating, the crystallites of the fcc-W$_2$N, fcc-NbN, and hexagonal NbN phases with an appropriate mutual orientation exhibit an interconnected arrangement. This interwind is a prerequisite for achieving semicoherence in crystallites.[73] Figure 4c−e
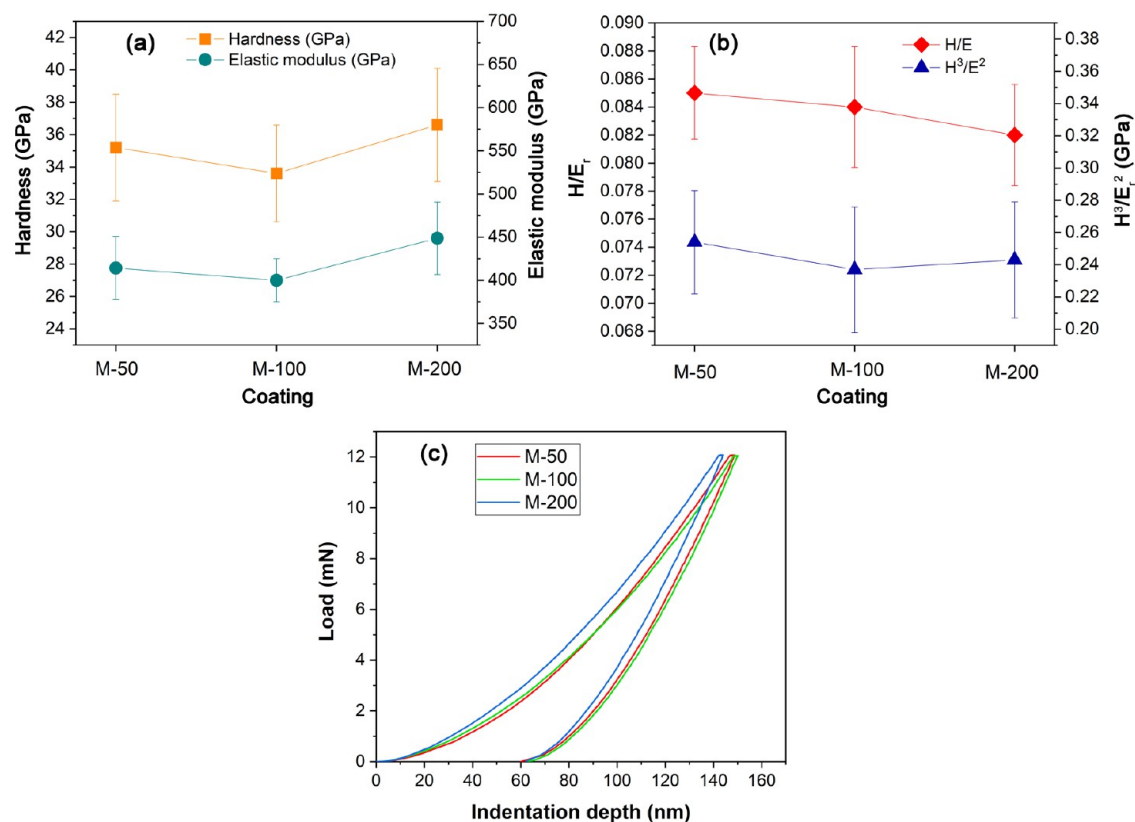
Figure 5. Hardness and elastic modulus (a), H/E_r and H^3/E_r^2 ratios (b), and typical load−displacement curves (c) from nanoindentation measurements of WN/NbN multilayer coatings deposited at different negative bias voltages.

demonstrates the corresponding EDS elemental mapping of the M-200 coating. Nitrogen was evenly distributed within the multilayer. Furthermore, a slight overlap between Nb and W was visible, confirming intermixing between different nitride layers during the deposition.

2.4. Mechanical Properties. The mechanical properties of the nanolayer nitride coatings were assessed by using nanoindentation tests. Four main parameters (nanohardness (H), elastic modulus (E_r), H/E_r, and H^3/E_r^2 ratios) were evaluated and are shown in Figure 5. Typical load−displacement curves of WN/NbN coatings are provided in Figure 5c. The hardness of the monolithic fcc W_2N was found to be within the range of 26.7−31.0 GPa.[34,46,49] The hexagonal ε-NbN and fcc δ-NbN coatings exhibited a hardness of 22−30 and 17−20 GPa, depending on the applied load.[54,66] Therefore, the hardness values of the deposited WN/NbN multilayer coatings clearly exceeded those of single-layer tungsten and niobium nitrides. The highest hardness (36.6 ± 3.5 GPa) and elastic modulus (448.7 ± 36.5 GPa) were observed for the M-200 sample. However, many authors have discussed the importance of high H/E_r and H^3/E_r^2 values for predicting wear-resistant properties.[38,74] The first parameter is connected to the energy dissipation in mechanical contact (elastic strain to failure), while the H^3/E_r^2 ratio is called the resistance to plastic deformation. The most durable protective coatings are expected to have high hardness in order to be effective in resisting plastic deformation and moderately low elastic modulus.[75,76] Hence, the highest values of H/E_r and H^3/E_r^2 ratios, as demonstrated by the M-50 multilayer, allowed us to suggest that it should exhibit an enhanced resistance to wear.

The deposited WN/NbN nanolayers demonstrated mechanical properties superior to those of their constituent monolayers due to a few mechanisms. First, the nanolayer architecture plays a crucial role in enhancing the mechanical properties. Due to the alternating deposition of the individual layers, multilayers have many interfaces that hinder crack propagation and dislocation movement throughout the coating. Such coatings have a significant area of interphase boundaries and many defects at the interfaces. Many papers that studied different multilayer films have demonstrated that there is an optimal bilayer period that provides the best mechanical properties. For example, TiN/WN coatings showed maximized hardness at Λ = 8.1 nm,[42] and an optimal bilayer period for NbN/WN multilayers was about 7.4 nm,[33] while in both cases, increasing the Λ deteriorated their characteristics. Similar behavior of the WN-based multilayer system was observed in the present study. The WN/NbN coating with the lowest Λ value of 10 nm (M-200) exhibited the highest hardness value of 36.6 ± 3.5 GPa. An increase in Λ to 13 nm (M-50) and 15 nm (M-100) led to a gradual decrease in hardness to 35.2 ± 3.3 and 33.6 ± 3.0 GPa, respectively. Another source of hardness enhancement is the lattice misfit between adjacent phases.[77,78] For instance, in the case of the M-200 coating, analysis of the FFT patterns provided in Figure 4 demonstrated that it was composed of three phases. Therefore, the lattice misfit for the crystallographic relationships along the $[0\bar{1}0]_{\varepsilon\text{-NbN}} \parallel [0\bar{1}1]_{\delta\text{-NbN}}$, $[0\bar{1}0]_{\varepsilon\text{-NbN}} \parallel [\bar{1}01]_{\beta\text{-W}_2\text{N}}$, and $[0\bar{1}1]_{\delta\text{-NbN}} \parallel [\bar{1}01]_{\beta\text{-W}_2\text{N}}$ interfaces were 4.1, 1.0, and 3.2%, respectively. All of the lattice mismatch values were positive, indicating an expansion of the unit cell of ε-NbN in the first two relationships and compression of crystal

lattices of cubic nitride phases. The δ-NbN/β-W$_2$N interface was also characterized by contraction of the niobium nitride lattice. This misfit is a source of the local strain at the phase boundaries, which is beneficial for the hardness.[78]

Another mechanism that could also be responsible for the high mechanical properties of the nanostructured WN/NbN coatings is a fine-grained structure. When the size of grains $d <$ 10 nm, dislocations do not appear if d is smaller than the length of a dislocation, and processes at the grain boundaries have a significant impact on the material properties.[79] Smaller grains mean an increase in grain boundaries that tend to accumulate dislocations and hinder their movement.[45] Moreover, the formation of the mixture of two different NbN phases also affected the mechanical properties. According to Pugh's criterion, if the Pugh modulus ratio k is greater than 1.75, the material demonstrates ductile behavior; otherwise, it has a brittle character. Papers studying different NbN polymorphs have shown that the calculated k value for ε-NbN was around 1.69, implying its brittle nature.[55,80] Yet the cubic δ-NbN demonstrated a much higher Pugh modulus ratio of about 2.20, indicating that it is a ductile material.[80,81] It should be considered that nanohardness measurements were conducted at a depth of about 200 nm. According to the phase analysis, this indicates that in the near-surface region, M-50 and M-200 coatings were characterized by a negligible amount of the ε-NbN phase and prevalent (111) orientation in most grains. Consequently, the presence of hard hexagonal nanocrystallites led to degradation of the mechanical properties. Conversely, the development of the (111) texture had a favorable impact. Hence, the M-50 coating's superior elastic strain to failure and resistance to plastic deformation were attributed to the synergy of small grain sizes, optimal texture, and bilayer period of 13 nm, and the lowest volume fraction of hard but brittle ε-NbN phase surrounded by a more ductile δ-NbN.

2.5. Tribological Tests. *2.5.1. Friction Performance.* The friction coefficient of the nanolayer WN/NbN coatings deposited at different substrate biases as a function of sliding time is listed in Figure 6. The running-in state of multilayers was short and characterized by a rapid increase in the COF. This is due to high contact stress and wear loss caused by the
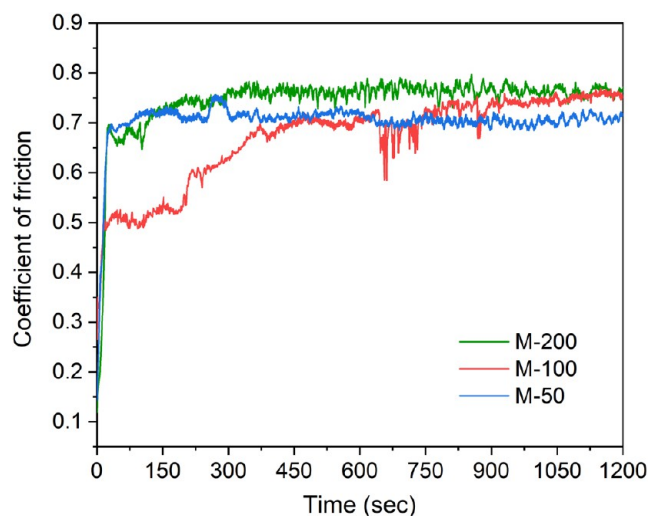
softening of the contact interfaces at the beginning of the dry sliding. Macroparticles at the surface of cathodic-arc evaporated coatings are droplets of target materials in the form of soft pure metals or hardened particles, which are created due to even a low efficiency of chemical reaction with nitrogen.[82] Such surface asperities during sliding act as abrasive particles that plow the coating surface and increase its wear. The surface roughness of three multilayers had similar values in the 37–41 nm range and was not a crucial factor responsible for different tribological test results. However, the friction behavior of the steady-state phase varied for different coatings.

The friction coefficient curve of the M-50 coating first had a slight ascending trend, with some spikes during the steady-state part up to 300 s of sliding. After the contact between the multilayer and steel counterbody surfaces was optimized, the COF decreased to approximately 0.7 and was stable until the end of the test. Therefore, when the steel ball slid over niobium nitride layers, hard and brittle ε-NbN nanograins surrounded by the δ-NbN phase could detach and refine, serving as an abrasive material. However, a negligible amount of hexagonal phase in this coating and the small average size of grains resulted in the lowest COF at longer distances.

The WN/NbN multilayer deposited at $U_s = -100$ V demonstrated no stable steady-state friction coefficient. After the running-in state, the COF constantly rose from 0.5 to 0.75, meaning a large scattering of the results. Even though this coating had the lowest average COF value of about 0.68, the friction behavior was irregular and unstable. The curve exhibited some discontinuity character with sharp fluctuations. That could be caused by local failure of the layer at some places or even minor coating delamination since the friction performance continued to worsen after those breakdown events. Moreover, another reason for those fluctuations in the COF could be related to a higher content of the hard ε-NbN grains, the particles of which potentially acted as a third body during the sliding process. During the sliding motion, they could be unevenly gathered at different parts of the wear track, expelled, or immersed within the transferred materials.

Finally, the steady state of the friction coefficient curve of the M-200 coating until 370 s had an ascending character, as observed for the M-50 sample. However, it stabilized for the rest of the sliding with some local fluctuations, which could be related to the alternate failure of different individual layers and continuous formation and removal of WO$_3$ and Nb$_2$O$_5$ tribo-oxides. This multilayer with the smallest Λ value of about 10 nm demonstrated the highest average COF value of 0.74. Zhang et al.[83] reported the same relation between the friction coefficient and bilayer period of CrSiN/ZrN coatings. The highest COF was observed for the coating with the smallest bilayer thickness.

The average friction coefficient of the monolithic NbN during the dry sliding against a stainless-steel ball was reported to be about 0.78.[32] The fcc W$_2$N coating deposited by magnetron sputtering demonstrated COF of about 0.47–0.5.[41,84] Thus, the CA-PVD WN/NbN coatings studied in this article showed friction coefficients with average values lying between those of individual constituent layers. Among all multilayers, the coating deposited at $U_s = -50$ V demonstrated the most stable friction performance, with the lowest COF at longer distances until the end of the sliding against a steel ball.

2.5.2. Wear Resistance. The wear behavior of CA-PVD WN/NbN coatings was assessed by ball-on-disk tests using a 100Cr6 stainless-steel counterbody. SEM images of the worn
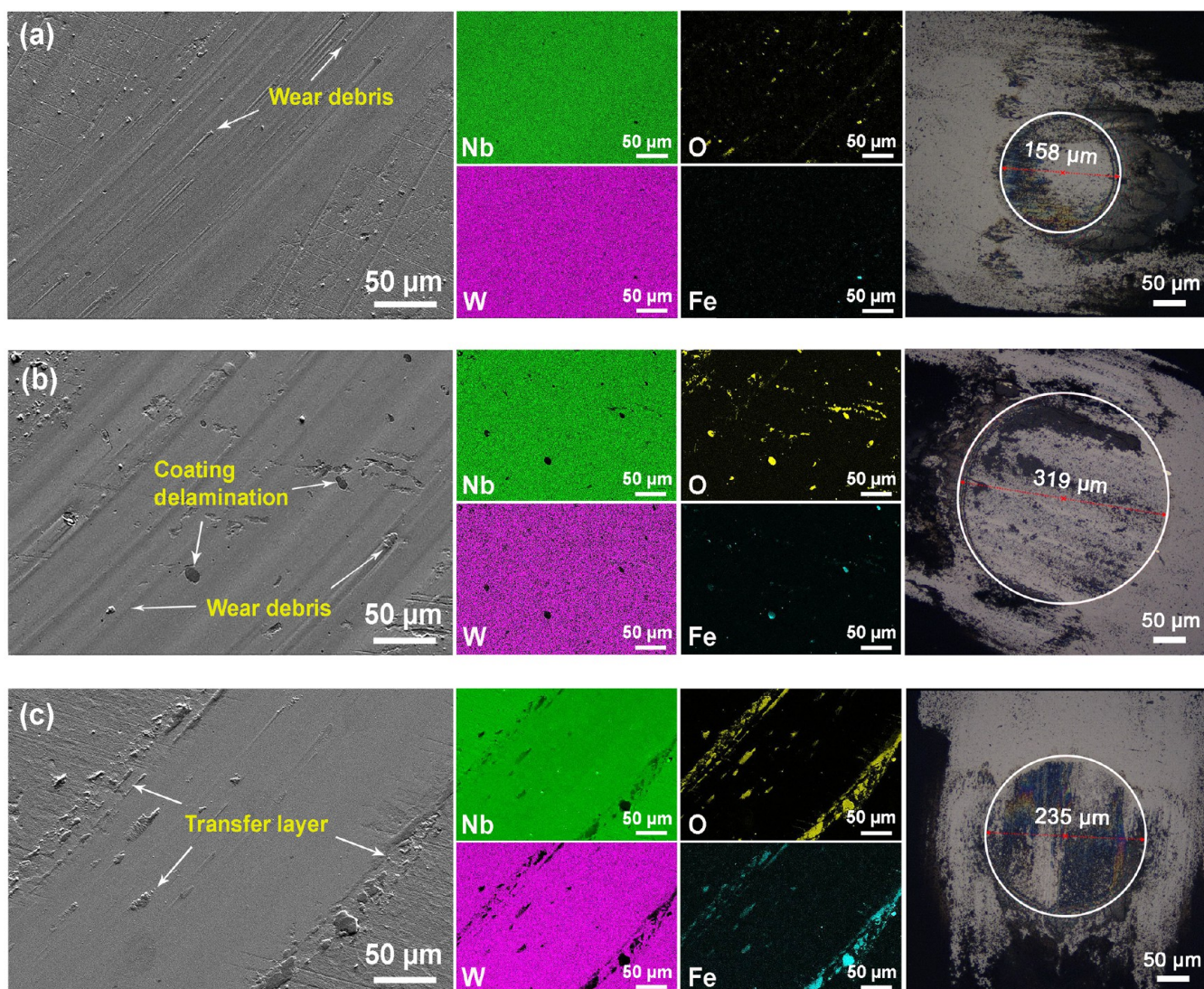
Figure 6. Evolution of the coefficient of friction of the WN/NbN multilayers deposited at various bias voltages depending on the sliding time against the steel ball.

Figure 7. SEM images of the wear tracks of the WN/NbN multilayers (first column), EDS elemental maps (smaller images in the middle), and images of 100Cr6 counterbody balls (last column) after ball-on-disk tribotests as a function of substrate bias: (a) −50, (b) −100, and (c) − 200 V.

surfaces of multilayers deposited at different substrate bias voltages and balls after tribotests are shown in Figure 7. EDS elemental maps were recorded to better understand the deposited coatings' main wear mechanisms. Signals from four elements were used for the analysis: tungsten, niobium, oxygen, and iron. The last two elements were indicators of the coating spallation with consequent substrate exposure and transfer layer formation from the steel counterbody on the wear scar surface. The M-50 and M-200 multilayers remained fully intact until the end of the wear tests. However, the M-100 sample exhibited a few areas of coating spallation with stainless-steel substrate exposure. Analysis of the wear scars of three CA-PVD WN/NbN coatings revealed different wear mechanisms and wear resistance.

The wear behavior is greatly influenced by a suitable combination of mechanical properties (hardness, elasticity, and resistance to plastic deformation), residual stresses, and microstructure (grain size, interfaces, and texture) of the coating.[85] Moreover, the thickness of the coating is one of the most essential parameters that affects its wear resistance and friction performance. For various materials, there is an optimal thickness that allows the reduction of wear, while the bilayer

period should also be optimized to improve the wear resistance in the case of multilayer coatings. Thus, these parameters were considered during the study of WN/NbN wear resistance, which was mainly assessed by calculating the specific wear rate, w_s. The w_s values of coatings deposited at different negative bias voltage values are provided in Figure 8.

The wear scar features of the WN/NbN coating deposited at $U_s = -50$ V are provided in Figure 7a. It can be seen that the M-50 multilayer exhibited the least damaged surface after sliding a steel ball for 75 m. The wear track was smooth without signs of coating delamination, and the scar profile was shallow, with width and depth of about 162 and 0.270 μm (Figure 9a). These parameters resulted in the lowest specific wear rate, 1.9×10^{-6} mm^3/Nm. Moreover, the wear scar on the counterbody after tribotests had the smallest size, and the wear rate of the ball was the lowest, with a value of 1.5×10^{-8} mm^3/Nm (Figure 8). Figure 7a shows only fine particles in small amounts. According to SEM-EDS elemental maps, those debris were oxides of tungsten and niobium, and no iron was detected on the wear scar area. These features indicate that the primary wear mechanism of the M-50 coating was oxidative wear (Figure 9b). Sliding two materials against each other
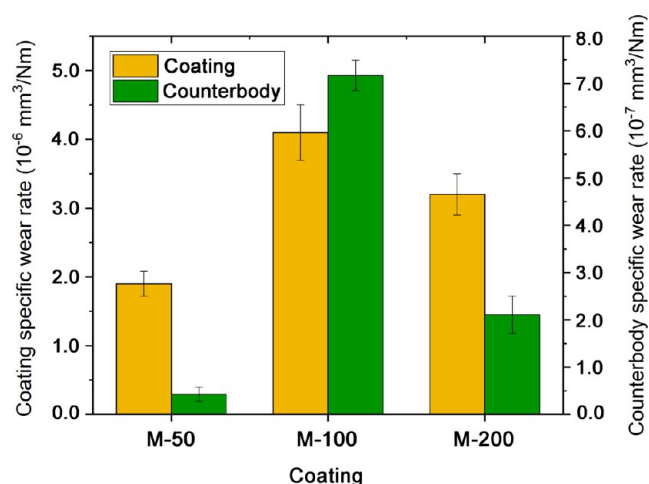
Figure 8. Specific wear rate values of WN/NbN coatings deposited various negative bias voltages and 100Cr6 steel counterbodies.

generates high temperatures in the tribe-pair contact. However, at low speeds below 1 m/s, the temperatures are not high enough to cause direct oxidation of the highest surface irregularities.[86] The process occurs due to the oxidation of accumulated wear debris. When oxide films grown on asperities reach a critical thickness of around a few nanometers, they detach from the worn surface in the form of flaky oxide wear particles that subsequently compact and create oxide "islands".[87,88] As sliding time increases, created plastically deformed oxides get flattened and smooth and may leave "tail-like" traces behind them. This type of wear mechanism is considered mild wear. Observed oxide wear particles could be WO_3 and Nb_2O_5, which are known for their lubricious properties. For instance, WO_3 is the Magnéli phase with a shear structure and lower shear strength.[25] It has lubricating properties due to three types of W−O bonds. This scale has a low hardness of about 5 GPa and can be worn easily during friction because of the weak van der Waals interactions between layers.[89] It can wear out fast but also takes a few microseconds to regrow. Therefore, WN can be considered a self-lubricating material. The NbN films showed similar behavior during wear tests. They can be oxidized to Nb_2O_5, which provides high wear resistance.[32,90] Thus, the formation of both tungsten and niobium oxides during the wear tests significantly improves the wear behavior of the deposited WN/NbN coatings. Moreover, the M-50 sample was characterized by the highest elastic strain to failure (H/E_r) and the highest resistance to plastic deformation (H^3/E_r^2), which also contributed to its superior wear resistance. These parameters indicated that the coating had an enhanced probability of elastic-dominated deformation, resistance to crack initiation, and load-carrying capacity.[91] This coating also had a high compressive residual stress, which is favorable for tribological applications since it may enhance mechanical properties and crack resistance.[92,93] Its wear behavior indicates that it had an optimal total thickness (4.7 μm) and bilayer period (13 nm) for sufficient load support to decrease the substrate deformation. The coating must be thick enough; otherwise, the soft substrate may not be able to carry the load and deform under the contact.

Analysis of SEM images of the wear track provided in Figure 7b and the scar profiles presented in Figure 9a of the M-100 multilayer revealed that it had the worst wear resistance. The

depth and width of the wear scar had the greatest values, which were attributed to the highest specific wear rate of 4.1×10^{-6} mm^3/Nm (Figure 8). However, it is still within the moderate wear range. Furthermore, the specific wear rate of the counterbody was also the highest (7.2×10^{-6} mm^3/Nm). As noted above, the resistance to plastic deformation, represented by the H^3/E_r^2 ratio, was the lowest for the M-100 multilayer (Figure 5b), which was found to be an indicator of low wear resistance. Moreover, the average bilayer period of this coating was higher than that for the coating deposited at −50 V (Λ = 15 nm), which could also be the reason for worse wear resistance. There is an optimal bilayer period that provides resistance to crack propagation. For instance, an investigation into the tribological and wear performance of HfN/VN nanolayers revealed enhanced hardness, decreased friction coefficient, and reduced wear at Λ = 15 nm.[94] Conversely, higher bilayer period values were found to compromise these properties. Furthermore, another reason contributing to the widest groove and coating delamination in the M-100 multilayer can be the highest amount of the brittle and hard hexagonal NbN phase, with an average grain size of about 4 nm (Table 3). Hard and small grains may act as hard inclusions. Their movement can promote the formation of voids, which grow in size as plastic deformation continues. Stresses below the wear zone are high, favoring the generation and propagation of cracks within the coating.[95] This, in turn, can lead to spalling, or even hard grains themselves can also be the sites that initiate delamination. These are features of fatigue wear. Nevertheless, the oxidative mode was present along with a fatigue wear mechanism, considering the SEM observations in Figure 7b. Compared with the coating deposited at a lower bias voltage, the M-100 multilayer exhibited a much higher number of larger oxides on the worn surface. Those wear debris were WO_3 and Nb_2O_5 "islands" formed during the tribochemical reaction of the WN and NbN layers with atmospheric oxygen. It should be noted that the formation of oxides can deteriorate the ability of the material to repair the crack through the adhesion of the fractured surfaces.[95] However, in this study, the resulting scales could also benefit wear resistance due to their lubricating properties. Thus, the synergy of these processes balanced severe fatigue wear, and the oxidative wear mechanism contributed to wear resistance improvement. A schematic illustration of the wear mechanisms involved is provided in Figure 9c.

The M-200 coating exhibited wear behavior different from that of the other WN/NbN multilayers. It demonstrated a smooth wear track with transfer layers on its surface, as seen in the SEM image (Figure 7c) and 3D profile image (Figure 9a). The width was approximately 240 nm, and the depth of the wear scar was measured to be around 363 nm. The calculated specific wear rate of the M-200 coating was about 3.2×10^{-6} mm^3/Nm. Thus, its wear resistance fell between those of the other two coatings. However, this multilayer exhibited a different wear behavior. The characteristic features of the M-200 wear track were transfer layers and fine wear particles. Therefore, the coating wear was caused by the synergy of two wear mechanisms: adhesive and oxidative. Adhesive wear is distinguished by material transfer from one surface (counterbody) to another (coating), with the formation of transfer films. When two materials are slid against each other, the formation of transfer particles is initially observed. However, as the sliding continues, these particles grow and become compacted and flattened, forming transfer layers. When
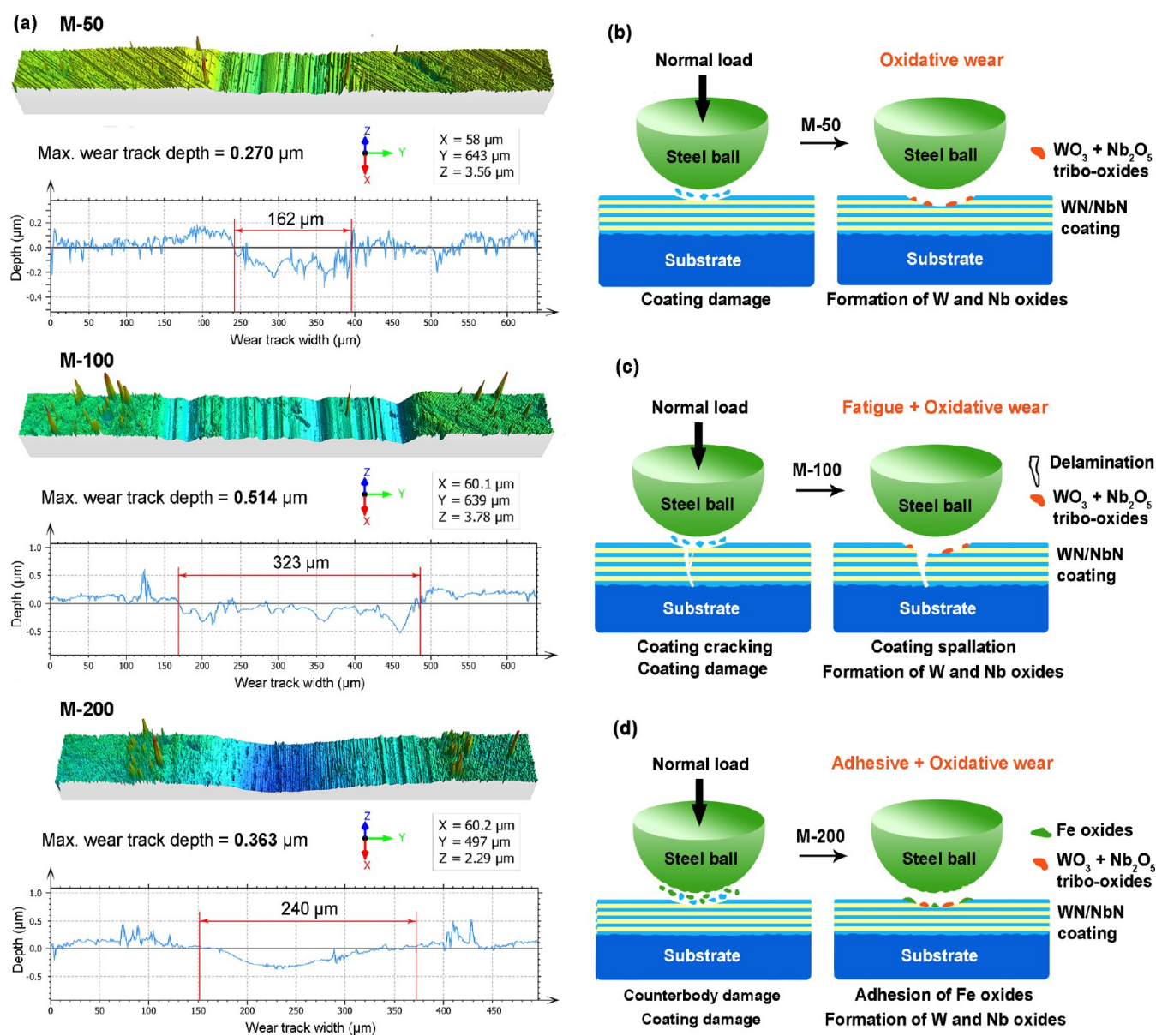
Figure 9. 2D and 3D profiles of wear tracks of the CA-PVD WN/NbN nanolayer coatings deposited at different bias voltages (a). Wear mechanisms of the M-50 (b), M-100 (c), and M-200 (d) multilayers.

exposed to air under atmospheric pressure, metals oxidize rapidly. These processes lead to the formation of thin oxide layers from transferred material on one of the sliding surfaces. The preferred areas for the adhesion of the transfer layer are the highest asperities of the coating.[85] The WN/NbN surface irregularities tended to tear off softer steel balls, and oxidized counterbody particles adhered to the coating without causing plowing or polishing effects. Hence, in the case of the M-200 multilayer, after sliding against a stainless-steel ball, the coating surface was covered in transfer layers consisting of iron oxides, indicating an adhesive wear mechanism. Those oxide particles were mainly located at the edges of the wear track but could also be seen inside the scar. Even though adhesive wear is considered a severe type of wear, it has been shown that Fe_3O_4 forming on the sliding surfaces acts as a protective oxide layer that reduces wear rate.[96] Moreover, the formation of adhesive layers can increase friction, which could be the reason for the higher friction coefficient of the M-200 coating (Figure 6).

Along with adhered transfer layers, wear particles of tungsten and niobium oxides were present. That indicated that along with adhesion wear the M-200 coating also demonstrated an oxidative wear mode (Figure 9d). On the smooth surface of the scar, no prominent grooves were observed created by soft W and Nb oxide particles. Similar to the other two multilayers, since the tribo-pair is exposed to the oxygen, fine metallic wear debris generated during the sliding gets oxidized and accretes with further formation of oxide wear debris. These WO_3 and $Nb_2O_{5,}$ in turn also act as lubricious protective oxide layers and reduce the severity of adhesive wear. Therefore, these factors resulted in the moderate value of the specific wear rate of the M-200 multilayer.

Furthermore, it should be taken into account that multilayer coatings were worn to different depths. Comparing the GIXRD patterns (Figure 3) and wear profiles (Figure 9a), we could study the relationship between the structural features and the wear resistance of WN/NbN multilayers. Thus, the M-50
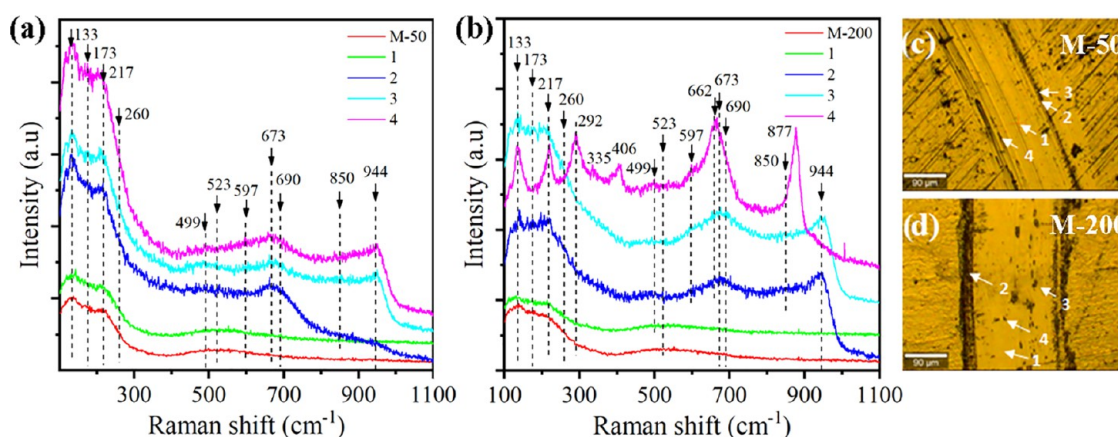
Figure 10. Raman spectra of WN/NbN multilayers deposited at a bias voltage of −50 (a) and −200 V (b), obtained from different areas indicated on micrographs (c, d): unworn coating surface (red spectra), flat area in the middle of the wear scar (spectra 1), wear debris at the edge (spectra 2), and inside of the wear track (spectra 3 and 4).

coating with the shallowest wear scar was worn out to about 270 nm from the surface. Such results meant that the structure of the sample involved in the wear process was characterized by a negligible amount of the hard ε-NbN phase, a (111) texture of the cubic grains with a small number of the (200)-oriented grains (Figure 2a). The deepest wear track was observed for the M-100 multilayer (about 514 nm). Notably, the phase composition remained almost unchanged throughout the studied coating thickness. It showed a (111) + (200) preferred orientation and the highest amount of hexagonal NbN. Finally, the M-200 coating was worn out to a thickness of 363 nm, where it still had a (111) texture of the fcc grains, but close to the end of the sliding, the fraction of ε-NbN slowly started to rise.

Hence, we can conclude that the specific wear rate was dependent on the presence of hard hexagonal grains. The higher the fraction of ε-NbN, the worse the wear resistance of the studied CA-PVD WN/NbN multilayers. Moreover, similar to the mechanical properties, the preferred orientation of cubic grains along the (111) plane had a positive impact on wear behavior. Analysis of the wear behavior of the CA-PVD WN/NbN coatings demonstrated that the optimal thickness and bilayer period, which provided the best wear resistance, were about 4.7 μm and 13 nm, respectively. Due to the high number of interfaces in the nanolayer architecture, small nanograins, negligible amount of hexagonal NbN crystallites, sufficient load-bearing capacity, high nanohardness, elastic strain to failure, and resistance to plastic deformation, the M-50 multilayer could effectively hinder crack propagation and withstand deformation and damage.

In order to prove the formation of tungsten and niobium oxides during the sliding process, Raman spectra of the M-50 and M-200 multilayers obtained from wear debris, the middle part and edges of wear tracks, and unworn coating surfaces were analyzed. All of the spectra of the deposited coatings presented in Figure 10 were characterized by a strong band in the range of 100−300 cm^{-1} and a weak band at 400−700 cm^{-1}. Notably, the first-order Raman active mode cannot be observed in the crystalline β-W$_2$N.[26,97] However, due to the presence of N vacancies, the broad bands reflected the vibration density of states and could be detected in the 150−350 cm^{-1} range with two double maximums at 155 and 209 cm^{-1}.[98] Moreover, different NbN phases can also be characterized by two distinct bands at 155−160 and 205−

210 cm^{-1}, whereas NbN$_x$ is represented by a broad frequency band with a maximum close to 100−190 cm^{-1}.[99,100] In turn, we suggested that the appearance of the strong Raman band in the range of 100−300 cm^{-1} with three distinct maximums at 133, 173, and 217 cm^{-1} could be related to NbN phases, as well as the nonstoichiometric WN$_x$ and NbN$_x$ on the WN/NbN interface.

Considering the weak Raman band at 400−700 cm^{-1}, the maximum of the band at 523 cm^{-1} could be assigned to the NbN$_x$,[99−101] whereas the broadening of the band could be an indication of the W$_2$N phase due to the shoulder at the higher wavenumbers (690 cm^{-1})[50] as well as WN$_x$ with a shoulder at 471 cm^{-1}.[98] The shoulder at 685 cm^{-1} observed in spectra 2 measured at the wear track edges tended to increase with the negative substrate bias voltage. That could indicate an increase in the W$_2$N phase and was in good agreement with the chemical composition and microstructural characteristics that suggest an enlargement of the W$_2$N crystallites.

All of the Raman spectra accumulated on the flat area in the middle part of the wear tracks (spectra 2) were very similar to those in the unworn region. An analysis of the wear debris inside and at the edges of the wear scars revealed very similar Raman spectra. Two strong bands were observed at 673 and 944 cm^{-1}, which could be related to Nb$_2$O$_5$ and WO$_3$ at 670[102] and 925−960 cm^{-1},[50,103] respectively. Notably, the small band at 850 cm^{-1} confirmed the formation of the Nb$_2$O$_5$.[102]

Moving to spectrum 4 of the M-200 multilayer, a group of peaks at 217, 292, 406, 499, 597, and 662 cm^{-1} were observed, which clearly indicated the α-Fe$_2$O$_3$.[104,105] In addition, the peak at 662 cm^{-1} could also be related to Fe$_3$O$_4$. The strong peaks centered at 877 and 662 cm^{-1} were attributed to the Fe−O−Cr interaction.[106] Thus, the analyzed debris could belong to the adhered particles transferred from the 100Cr6 steel ball during sliding. However, Raman spectra of the wear debris from the M-50 multilayer did not show such peaks. This coating had only small visible bands at 499 and 597 cm^{-1}. In that case, the intensity of those bands was relatively small, and all other bands related to the α-Fe$_2$O$_3$ were not detected; thus, we could assign them to the O−W−O[107] vibrations and amorphous Nb$_2$O$_5$,[108] respectively. Finally, a strong increase of the peak at 133 cm^{-1} at the spectra obtained from the worn surfaces could be caused by the rise in the WO$_3$ or Nb$_2$O$_5$ phases.

Raman spectroscopy, therefore, confirmed that the M-200 coating was characterized by adhesive and oxidative wear mechanisms with iron oxides transferred from a steel counterbody as well as Nb_2O_5 and WO_3 formed at the worn surface. In contrast, the primary wear mode of the M-50 multilayer was solely oxidative wear in the presence of lubricating WO_3 or Nb_2O_5 tribo-oxides, which contributed to enhanced wear resistance.

3. CONCLUSIONS

In summary, changes in structural features, mechanical properties, friction performance, and wear resistance of the cathodic-arc evaporated WN/NbN coatings deposited at various energies of bombarding ions have been comprehensively investigated. Applying a negative bias voltage in the 50−200 V range resulted in variations in the total coating thickness (3.5−5.0 μm) and bilayer period (10−15 nm) of the deposited multilayers. WN/NbN multilayers demonstrated a tendency for (111)-oriented grains to overgrow the (200)-oriented grains with increasing coating thickness to varying degrees. Notably, the lower the bilayer period, the more drastic the changes in the preferred orientation were observed. Analysis of the relationship between the microstructure and tribomechanical properties revealed that the formation of hard hexagonal grains and the (111) preferred orientation had negative and positive effects, respectively. As the absolute value of the negative bias voltage increased, the wear mechanisms changed: oxidative → fatigue + oxidative → adhesive + oxidative. Oxidative wear contributed to better wear resistance.

Furthermore, the coating deposited at the lowest negative bias voltage of −50 V exhibited superior wear resistance with the lowest specific wear rate of 1.9×10^{-6} mm^3/Nm. This was attributed to the optimal thickness, bilayer period, high number of interfaces, small nanograins, the formation of lubricating Nb_2O_5 and WO_3, low volume fraction of the hexagonal NbN phase, and (111)-oriented grains as well as high nanohardness (35.2 ± 3.3 GPa), elastic strain to failure, and resistance to plastic deformation. Thus, based on the conducted analysis, it could be stated that elaborated CA-PVD WN/NbN nanolayer coatings hold significant promise as high-potential protective coatings suitable for tribological applications.

4. EXPERIMENTAL SECTION

4.1. Coating Deposition Process. For this study, three WN/NbN nanolayer coatings were deposited by a cathodic-arc evaporation method by using an upgraded "Bulat-6" device. The schematic illustration of the deposition equipment is provided in Figure 11. W (99.5%) and Nb (99.5%) were used as targets for the coating synthesis. The angle between two cathodes was set at 90° in the vacuum chamber. The substrate material was X6CrNiTi18-11 stainless steel. Before the deposition process, substrates were mechanically ground, polished on a polishing cloth with Goya's paste, and ultrasonically cleaned in acetone and alcohol. They were then sputter-cleaned in an argon plasma for 10 min to eliminate surface impurities and the oxide layer. Three WN/NbN coatings were prepared in a nitrogen atmosphere by changing the negative substrate bias voltage, U_s. Multilayers deposited at −50, −100, and −200 V were designated M-50, M-100, and M-200, respectively. In order to synthesize a nanolayer architecture, the substrate holder was constantly
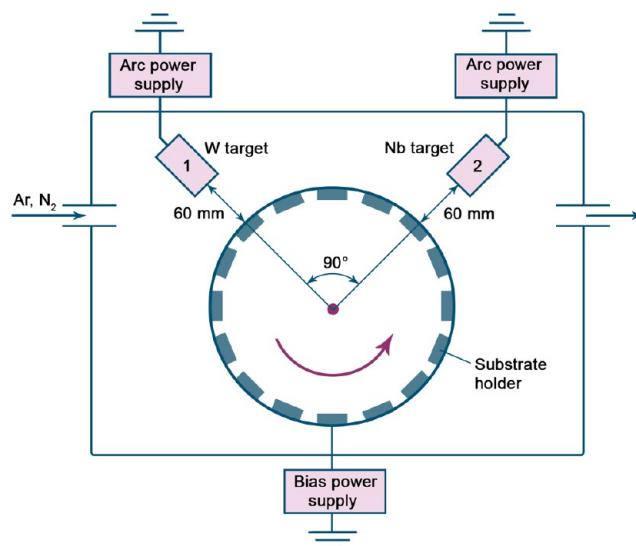

Figure 11. Schematic illustration of upgraded "Bulat-6" cathodic-arc evaporation equipment.

rotated at a rate of 7 rpm so that substrates alternately faced different targets. The distance between the substrate and each target was kept at 60 mm. The working gas pressure was maintained at 0.4 Pa. The temperature of the substrate during the deposition process was fixed at 400 °C. The arc current applied to the W and NbN targets was 120 A. The total time of coating deposition was maintained at 60 min.

4.2. Microstructure and Surface Characterization. The phase analysis of the deposited WN/NbN coatings was assessed using Grazing incident X-ray diffractometry (GIXRD, Panalytical Empyrean X-ray diffractometer). The X-ray radiation source was Cu Kα (Λ = 0.15406 nm) operated at I = 40 mA and U = 40 kV. The incident angle ω was fixed at 0.5, 1, 4, 8, and 10°. The measurements were collected within the 2Theta interval from 20 to 90° at a step size of 0.1°. The path of the incident beam was composed of a parallel beam X-ray mirror for Cu-radiation, with a 0.04 rad. Soller slit, a fixed 1/16° divergence slit, and a 10 mm fixed mask. The path of the diffracted beam consisted of 0.04 rad. Soller slit, 0.27° slit parallel plate collimator, parallel plate collimator slit, and scintillation point detector. The average crystallite sizes were calculated using GIXRD patterns collected at ω = 8° using the Scherrer equation

$$D = K \cdot \Lambda / \beta \cdot \cos \theta$$

where D is the crystallite size, K is a function of the crystallite shape (0.9), Λ is the wavelength of the Cu Kα X-ray radiation source, β is the full width at half-maximum (FWHM) of the analyzed peak, and θ is the diffraction angle.

Residual stresses were evaluated via $\sin^2 \psi$ measurements using a Panalytical Empyrean X-ray diffractometer using a Co X-ray tube ($\lambda_{K\alpha_1}$ = 0.178901 nm). The incident beam was introduced through a parallel beam mirror, iron β-filter, a 1 mm mask, and a fixed divergence slit. The diffracted beam pathed through a 0.04 rad. Soller slit, 0.27° slit parallel plate collimator, parallel plate collimator slit, and a proportional Xe point detector. The (311) peak was selected for stress measurements of the M-50 and M-100 multilayers. The 2θ interval ranged from 79 to 99°, while for the M-200 coating, the scan range was 40−60° in order to evaluate residual

stresses using (111) and (200) planes since other peaks were missing.

The cross-sectional morphology of multilayers was analyzed using a JEOL JSM 7600F high-resolution field emission scanning electron microscope (SEM, JEOL), which was operated in the backscatter electron (BSE) imaging mode. In order to prepare the cross sections, samples were mechanically ground and polished. Wavelength-dispersive X-ray spectroscopy (WDS) was employed to study the chemical composition of coatings using the Oxford Instruments Inca Wave spectrometer installed in SEM. Before a quantitative analysis of the WN/NbN system was conducted, the WDS spectrometer underwent calibration using standards of BN, W, and Nb. For X-ray data quantification, the $K\alpha$, $L\alpha$, and $M\alpha$ lines were chosen for nitrogen, niobium, and tungsten, respectively.

The lamella of the WN/NbN coating deposited at $U_s = -200$ V (M-200) was prepared by the Nanoanalytik Zeiss Auriga 60 high-resolution focused ion beam scanning electron microscope (FIB-SEM). Initially, a protective multilayer consisting of platinum and carbon with dimensions of 20 μm $\times$ 2 μm $\times$ 2 μm was deposited on the surface. Subsequently, to mitigate the impact of inherent stresses and prevent lamella breakage, rectangular trenches, about 1 μm in width, were precisely cut. Following this, the lamella was thinned out using an ion beam to approximately 1 μm. The following steps involved mounting the lamella onto a TEM copper grid and performing a final thinning with beam currents changing from 600 pA down to 50 pA at 30 kV, followed by a finishing polish using a low current beam. Nanoscale microstructure features of the M-200 coating were investigated by using a double-corrected field emission atomic resolution analytical TEM JEOL JEM-ARM200CF (200 kV). High-resolution TEM (HR-TEM) and STEM images analyzed in this paper were recorded in the following modes: bright-field (BF), low-angle annular dark-field (LAADF), and high-angle annular dark-field (HAADF). The inner-collection angles of the LAADF and HAADF detectors were set at 35 and 90 mrad, respectively. Gatan DigitalMicrograph and CrysTBox software were utilized for data processing.

Raman spectra were measured using the WiTeC Alpha 300R microRaman system with a laser source of 532 nm wavelength with 1 mW power. In all sample areas, they were collected during the integration time of 15 s and were accumulated 20 times.

4.3. Tribomechanical Properties. The nanohardness and elastic modulus values of the WN/NbN coatings were measured by using the Anton Paar NHT2 nanoindenter with a Berkovich indenter tip. The maximum load applied during the test was 12 mN, with a loading/unloading rate of about 48 mN/min. The dwell time was fixed at 5 s. The hardness value was calculated as an average of 16 measurements for each sample.

The ball-on-disk tests were conducted to evaluate the coefficient of friction (COF) and resistance to wear by using a Bruker UMT Tribolab Tribometer. A ball made of 100Cr6 high-carbon-bearing steel with a diameter of 6.3 mm utilized as a counterbody slid against the WN/NbN coating surface for 200 s. An applied normal load was set at 3 N, the velocity was fixed at 200 rpm, and the track radius was 2.5 mm. This resulted in a total sliding distance of 75 m. Tribological tests were repeated three times under ambient room temperature (22−23 °C) and relative humidity of 38−42%. The ASTM

G99-17 standard was considered for the calculation of the specific wear rate using the following equation:

$$w_s = V/F \cdot L$$

where V is the volume loss, F is the applied normal load, and L is the sliding distance.

The wear volume of the coating was determined using the following equation

$$V_{coat} = \pi \cdot R(S_1 + S_2 + S_3 + S_4)/2$$

where R is the radius of the wear track and $S_1 - S_4$ are cross-sectional areas at four places on the wear track at intervals of 90°. The wear volume of the ball specimen was calculated as follows:

$$V_{ball} = \pi A^3 B/32D$$

where A is the minimum diameter of the wear scar, B is the diameter in a direction perpendicular to the minimum diameter, and D is the diameter of the ball counterbody.

Zeiss LSM 700 scanning laser confocal microscope (LSCM) was employed to evaluate the wear volume of the WN/NbN nanolayer coatings. The 3D maps of the wear track profiles were created by stitching and processing the data using Zeiss ConfoMap Premium 7.2 software.

■ AUTHOR INFORMATION

Corresponding Author

Kateryna Smyrnova − *Institute of Materials Science, Slovak University of Technology in Bratislava, 917 24 Trnava, Slovak Republic; Biomedical Research Centre, Sumy State University, 40007 Sumy, Ukraine;* Present Address: Biomedical Research Centre, Sumy State University, Rymskogo-Korsakova St. 2, 40007 Sumy, Ukraine; orcid.org/0000-0001-8993-996X; Email: kateryna.v.smyrnova@gmail.com

Authors

Martin Sahul − *Institute of Materials Science, Slovak University of Technology in Bratislava, 917 24 Trnava, Slovak Republic*

Marián Haršáni − *Research and Development Department, 038 53 Turany, Slovak Republic*

Vyacheslav Beresnev − *Department of Reactor Engineering Materials and Physical Technologies, V.N. Karazin Kharkiv National University, 61022 Kharkiv, Ukraine*

Martin Truchlý − *Department of Experimental Physics, Comenius University in Bratislava, 842 48 Bratislava, Slovak Republic;* orcid.org/0000-0001-9790-8522

Ľubomír Čaplovič − *Institute of Materials Science, Slovak University of Technology in Bratislava, 917 24 Trnava, Slovak Republic*

Mária Čaplovičová − *Centre for Nanodiagnostics of Materials, Slovak University of Technology in Bratislava, 812 43 Bratislava, Slovak Republic*

Martin Kusý − *Institute of Materials Science, Slovak University of Technology in Bratislava, 917 24 Trnava, Slovak Republic*

Andrii Kozak − *Institute of Electrical Engineering, Slovak Academy of Sciences, 841 04 Bratislava, Slovak Republic;* orcid.org/0000-0003-4226-8737

Dominik Flock − *Institute of Materials Science and Engineering, Ilmenau University of Technology, 98693 Ilmenau, Germany*

Alexey Kassymbaev − *Center of Advanced Development "VERITAS", D. Serikbayev East Kazakhstan State Technical University, 070004 Ust-Kamenogorsk, Kazakhstan*

Alexander Pogrebnjak − *Institute of Materials Science, Slovak University of Technology in Bratislava, 917 24 Trnava, Slovak Republic; Biomedical Research Centre, Sumy State University, 40007 Sumy, Ukraine;* ⊙ orcid.org/0000-0002-9218-6492

Complete contact information is available at:
https://pubs.acs.org/10.1021/acsomega.3c10242

Notes

The authors declare no competing financial interest.

■ REFERENCES

(1) Schleinkofer, U.; Czettl, C.; Michotte, C. Coating Applications for Cutting Tools. In *Comprehensive Hard Materials*; Elsevier, 2014; pp 453−469.

(2) Rizzo, A.; Goel, S.; Luisa Grilli, M.; Iglesias, R.; Jaworska, L.; Lapkovskis, V.; Novak, P.; Postolnyi, B. O.; Valerini, D. The Critical Raw Materials in Cutting Tools for Machining Applications: A Review. *Materials* 2020, 13 (6), 1377.

(3) Draher, T.; Polakovic, T.; Li, J.; Li, Y.; Welp, U.; Jiang, J. S.; Pearson, J.; Armstrong, W.; Meziani, Z.-E.; Chang, C.; Kwok, W.-K.; Xiao, Z.; Novosad, V. Ion-Beam Assisted Sputtering of Titanium Nitride Thin Films. *Sci. Rep.* 2023, 13 (1), 6315.

(4) Warcholinski, B.; Gilewicz, A.; Myslinski, P.; Dobruchowska, E.; Murzynski, D. Structure and Properties of AlCrN Coatings Deposited Using Cathodic Arc Evaporation. *Coatings* 2020, 10 (8), 793.

(5) Faraji, G.; Kim, H. S.; Kashi, H. T. Introduction. In *Severe Plastic Deformation*; Elsevier, 2018; pp 1−17.

(6) Rane, A. V.; Kanny, K.; Abitha, V. K.; Thomas, S. Methods for Synthesis of Nanoparticles and Fabrication of Nanocomposites. In *Synthesis of Inorganic Nanomaterials*; Elsevier, 2018; pp 121−139.

(7) Li, Z.; Khor, K. A. Preparation and Properties of Coatings and Thin Films on Metal Implants. In *Encyclopedia of Biomedical Engineering*; Elsevier, 2019; pp 203−212.

(8) Makhlouf, A. S. H. Current and Advanced Coating Technologies for Industrial Applications. In *Nanocoatings and Ultra-Thin Films*; Woodhead Publishing, 2011; pp 3−23.

(9) Matthews, A. Titanium Nitride PVD Coating Technology. *Surf. Eng.* 1985, 1 (2), 93−104.

(10) Bobzin, K. High-Performance Coatings for Cutting Tools. *CIRP J. Manuf. Sci. Technol.* 2017, 18, 1−9.

(11) Vopát, T.; Sahul, M.; Haršáni, M.; Vortel, O.; Zlámal, T. The Tool Life and Coating-Substrate Adhesion of AlCrSiN-Coated Carbide Cutting Tools Prepared by LARC with Respect to the Edge Preparation and Surface Finishing. *Micromachines* 2020, 11 (2), 166.

(12) Umezaki, Y.; Funaki, Y.; Kurokawa, S.; Ohnishi, O.; Doi, T. Wear Resistance of Coating Films on Hob Teeth: (Intermittent Cutting Tests with a Flytool). *JAMDSM* 2012, 6 (2), 206−221.

(13) Liu, Y.; Yu, S.; Shi, Q.; Ge, X.; Wang, W. Multilayer Coatings for Tribology: A Mini Review. *Nanomaterials* 2022, 12 (9), 1388.

(14) Pogrebnjak, A.; Smyrnova, K.; Bondar, O. Nanocomposite Multilayer Binary Nitride Coatings Based on Transition and Refractory Metals: Structure and Properties. *Coatings* 2019, 9 (3), 155.

(15) Zhou, C.; Wang, J.; Meng, J.; Li, W.; Liu, P.; Zhang, K.; Ma, F.; Ma, X.; Feng, R.; Liaw, P. K. Effects of Modulation Layer Thickness on Fracture Toughness of a TiN/AlN-Ni Multilayer Film. *Mater. Des.* 2022, 222, No. 111097.

(16) Pogrebnjak, A.; Buranich, V.; Ivashchenko, V.; Baimoldanova, L.; Rokosz, K.; Raaen, S.; Zukowski, P.; Opielak, M.; Rakhadilov, B.; Beresnev, V.; Erdybaeva, N. The Effect of Substrate Treatment on the Properties of TiAlSiYN/CrN Nanocomposite Coatings. *Surf. Interfaces* 2022, 30, No. 101902.

(17) Du, J. W.; Chen, L.; Chen, J.; Du, Y. Mechanical Properties, Thermal Stability and Oxidation Resistance of TiN/CrN Multilayer Coatings. *Vacuum* 2020, 179, No. 109468.

(18) Atmani, T. D.; Bouamerene, M.-S.; Gaceb, M.; Nouveau, C.; Aknouche, H. Improvement of the Tribological Behavior of TiN/CrN Multilayer Coatings by Modulation Wavelength Variation. *Tribol. Int.* 2024, 192, No. 109226.

(19) Huang, Y.; Chen, Z.; Wagner, A.; Mitterer, C.; Song, K.; Zhang, Z. High Density of Stacking Faults Strengthened TaN/TiN Multilayer. *Acta Mater.* 2023, 255, No. 119027.

(20) Gao, Z.; Buchinger, J.; Koutná, N.; Wojcik, T.; Hahn, R.; Mayrhofer, P. H. Ab Initio Supported Development of TiN/MoN Superlattice Thin Films with Improved Hardness and Toughness. *Acta Mater.* 2022, 231, No. 117871.

(21) Hovsepian, P. E.; Ehiasarian, A. P.; Purandare, Y. P.; Mayr, P.; Abstoss, K. G.; Mosquera Feijoo, M.; Schulz, W.; Kranzmann, A.; Lasanta, M. I.; Trujillo, J. P. Novel HIPIMS Deposited Nano-structured CrN/NbN Coatings for Environmental Protection of Steam Turbine Components. *J. Alloys Compd.* 2018, 746, 583−593.

(22) Pogrebnjak, A. D.; Beresnev, V. M.; Bondar, O. V.; Postolnyi, B. O.; Zaleski, K.; Coy, E.; Jurga, S.; Lisovenko, M. O.; Konarski, P.; Rebouta, L.; Araujo, J. P. Superhard CrN/MoN Coatings with Multilayer Architecture. *Mater. Des.* 2018, 153, 47−59.

(23) Moharana, P. L.; Anwar, S.; Islam, A.; Anwar, S. Structural and Mechanical Study of Thermally Annealed Tungsten Nitride Thin Films. *Perspect. Sci.* 2016, 8, 636−638.

(24) Ghantasala, S. B.; Sharma, S. Synthesis and Characterisation of Self-Lubricating Tungsten Nitride Thin Films as Protective Machine Tool Coatings. *Trans. IMF* 2024, 102 (1), 50−56.

(25) Javdošňák, D.; Musil, J.; Soukup, Z.; Haviar, S.; Čerstvý, R.; Houska, J. Tribological Properties and Oxidation Resistance of Tungsten and Tungsten Nitride Films at Temperatures up to 500 °C. *Tribol. Int.* 2019, 132, 211−220.

(26) Castaldo, A.; Gambale, E.; Iemmo, L. Thermal Stability of Sputtered Tungsten Nitrides for Solar Thermal Applications. *Appl. Sci.* 2022, 12 (20), 10208.

(27) Polcar, T.; Cavaleiro, A. Structure, Mechanical Properties and Tribology of W−N and W−O Coatings. *Int. J. Refract. Met. Hard Mater.* 2010, 28 (1), 15−22.

(28) Polcar, T.; Parreira, N. M. G.; Cavaleiro, A. Structural and Tribological Characterization of Tungsten Nitride Coatings at Elevated Temperature. *Wear* 2008, 265 (3−4), 319−326.

(29) Rehman, S. U.; Khan, S. A.; Uddin, W.; Khan, Q. U.; Kiani, M.; Mehmood, I.; Sohail, M.; Saeed, M.; Kumar, S.; Zhu, L. First Principle Study of New W2N Monolayer: A Promising Candidate for Li+ Ion Batteries. *Int. J. Electrochem. Sci.* 2019, 14 (3), 3070−3080.

(30) Smyrnova, K.; Sahul, M.; Haršáni, M.; Pogrebnjak, A.; Ivashchenko, V.; Beresnev, V.; Stolbovoy, V.; Čaplovič, L'.; Čaplovičová, M.; Vančo, L'.; Kusý, M.; Kassymbaev, A.; Satrapinskyy, L.; Flock, D. Microstructure, Mechanical and Tribological Properties of Advanced Layered WN/MeN (Me = Zr, Cr, Mo, Nb) Nanocomposite Coatings. *Nanomaterials* 2022, 12 (3), 395.

(31) Singh, K.; Krishnamurthy, N.; Suri, A. K. Adhesion and Wear Studies of Magnetron Sputtered NbN Films. *Tribiol. Int.* **2012**, *50*, 16−25.

(32) Miao, K.; Wang, J.; Zhao, Q.; Wang, K.; Wen, M.; Zhang, K. Water-Based Lubrication of Niobium Nitride. *Friction* **2022**, *10* (6), 842−853.

(33) Wen, M.; Tian, H. W.; Hu, C. Q.; Zeng, Y.; Meng, Q. N.; Zhang, K.; Zheng, W. T.; An, T.; Zou, G. T. Modulation Periodicity Dependent Structure, Stress, and Hardness in NbN/W 2 N Nanostructured Multilayer Films. *J. Appl. Phys.* **2011**, *109* (12), No. 123525.

(34) Wang, M. X.; Zhang, J. J.; Yang, J.; Wang, L. Q.; Li, D. J. Influence of Ar/N2 Flow Ratio on Structure and Properties of Nanoscale ZrN/WN Multilayered Coatings. *Surf. Coat. Technol.* **2007**, *201* (9), 5472−5476.

(35) Wu, F.-B.; Tien, S.-K.; Lee, J.-W.; Duh, J.-G. Comparison in Microstructure and Mechanical Properties of Nanocomposite CrWN and Nanolayered CrN/WN Coatings. *Surf. Coat. Technol.* **2006**, *200* (10), 3194−3198.

(36) Wu, F.-B.; Tien, S.-K.; Duh, J.-G. Manufacture, Microstructure and Mechanical Properties of CrWN and CrN/WN Nanolayered Coatings. *Surf. Coat. Technol.* **2005**, *200* (5−6), 1514−1518.

(37) Tsai, Y.-Z.; Duh, J.-G. Tribological Behavior of CrN/WN Multilayer Coatings Grown by Ion-Beam Assisted Deposition. *Surf. Coat. Technol.* **2006**, *201* (7), 4266−4272.

(38) Li, R. L.; Tu, J. P.; Hong, C. F.; Liu, D. G.; Sun, H. L. Microstructure, Mechanical and Tribological Properties of CrN/W2N Multilayer Films Deposited by DC Magnetron Sputtering. *Surf. Coat. Technol.* **2009**, *204* (4), 470−476.

(39) Kumar, D. D.; Kumar, N.; Kalaiselvam, S.; Dash, S.; Jayavel, R. Wear Resistant Super-Hard Multilayer Transition Metal-Nitride Coatings. *Surf. Interfaces* **2017**, *7*, 74−82.

(40) Ye, F.; Zhao, H.; Tian, X. The Elevated-Temperature Wear Properties of TiN and TiN/W 2 N Coatings. *Mater. Res. Express* **2018**, *5* (10), No. 106404.

(41) Chang, C.-L.; Chiou, T.-H.; Chen, P.-H.; Chen, W.-C.; Ho, C.-T.; Wu, W.-Y. Characteristics of TiN/W2N Multilayers Prepared Using Magnetron Sputter Deposition with Dc and Pulsed Dc Powers. *Surf. Coat. Technol.* **2016**, *303*, 25−31.

(42) Buchinger, J.; Koutná, N.; Chen, Z.; Zhang, Z.; Mayrhofer, P. H.; Holec, D.; Bartosik, M. Toughness Enhancement in TiN/WN Superlattice Thin Films. *Acta Mater.* **2019**, *172*, 18−29.

(43) Bodnarchuk, V. I.; Petrov, P.; Kozlenko, D. P.; Dechev, D.; Ivanov, N.; Martev, I.; Kasatkin, I. A. Study into the Properties of TiN/WN Multilayer Nanocoatings Prepared via Magnetron Sputtering. *J. Surf. Invest.: X-Ray, Synchrotron Neutron Tech.* **2017**, *11* (1), 186−189.

(44) Sahul, M.; Bočáková, B.; Smyrnova, K.; Haršáni, M.; Sahul, M.; Truchlý, M.; Kusý, M.; Pogrebnjak, A.; Čaplovič, L'.; Vopát, T. The Influence of Multilayer Architecture on the Structure and Mechanical Properties of WN x /TiSiN Coatings in Comparison with WN x and TiSiN Single Layers. *J. Phys.: Conf. Ser.* **2022**, *2413* (1), No. 012013.

(45) Xu, X.; Su, F.; Li, Z. Tribological Properties of Nanostructured TiAlN/W2N Multilayer Coating Produced by PVD. *Wear* **2019**, *430−431*, 67−75.

(46) Chan, Y.-C.; Chen, H.-W.; Tsai, Y.-Z.; Duh, J.-G.; Lee, J.-W. Texture, Microstructure and Anti-Wear Characteristics in Isostructural CrAlSiN/W2N Multilayer Coatings. *Thin Solid Films* **2013**, *544*, 265−269.

(47) Tsai, Y.-Z.; Duh, J.-G. Tribological Behavior of CrAlSiN/W2N Multilayer Coatings Deposited by DC Magnetron Sputtering. *Thin Solid Films* **2010**, *518* (24), 7523−7526.

(48) Tsai, Y. Z.; Duh, J. G. Enhanced Hardness of CrAlSiN/W 2 N Superlattice Coatings Deposited by Direct Current Magnetron Sputtering. *J. Mater. Res.* **2010**, *25* (12), 2325−2329.

(49) Duan, J.; Ye, F.; Zhao, H. The Study of the Tribological Properties of TiAgN/W 2 N Coatings in a Wide Temperature Range. *Mater. Res. Express* **2019**, *6* (8), No. 086407.

(50) Zhao, H.; Mu, C.; Ye, F. The Effect of Modulation Period on the Mechanical and Wear Properties of TiAgN/W2N Coatings. *Surf. Coat. Technol.* **2017**, *309*, 29−34.

(51) Bagdasaryan, A. A.; Pshyk, A. V.; Coy, L. E.; Kempiński, M.; Pogrebnjak, A. D.; Beresnev, V. M.; Jurga, S. Structural and Mechanical Characterization of (TiZrNbHfTa)N/WN Multilayered Nitride Coatings. *Mater. Lett.* **2018**, *229*, 364−367.

(52) Chang, Y.-Y.; Chao, L.-C. Effect of Substrate Bias Voltage on the Mechanical Properties of AlTiN/CrTiSiN Multilayer Hard Coatings. *Vacuum* **2021**, *190*, No. 110241.

(53) Terao, N. Structure Des Nitrures de Niobium. *Jpn. J. Appl. Phys.* **1965**, *4* (5), 353.

(54) Zou, Y.; Qi, X.; Zhang, C.; Ma, S.; Zhang, W.; Li, Y.; Chen, T.; Wang, X.; Chen, Z.; Welch, D.; Zhu, P.; Liu, B.; Li, Q.; Cui, T.; Li, B. Discovery of Superconductivity in Hard Hexagonal ε-NbN. *Sci. Rep.* **2016**, *6* (1), No. 22330.

(55) Ivashchenko, V. I.; Turchi, P. E. A.; Pavlova, N. Y.; Gorb, L.; Leszczynski, J. Temperature- and Pressure-Induced Structural Transformations in NbN: A First-Principles Study. *Phys. B* **2023**, *663*, No. 414998.

(56) Linde, A. V.; Marin-Ayral, R.-M.; Granier, D.; Bosc-Rouessac, F.; Grachev, V. V. Synthesis of Cubic Niobium Nitride by Reactive Diffusion under Nitrogen Pressure. *Mater. Res. Bull.* **2009**, *44* (5), 1025−1030.

(57) Hones, P.; Martin, N.; Regula, M.; L vy, F. Structural and Mechanical Properties of Chromium Nitride, Molybdenum Nitride, and Tungsten Nitride Thin Films. *J. Phys. D: Appl. Phys.* **2003**, *36* (8), 1023−1029.

(58) Cheng, Y. H.; Tay, B. K.; Lau, S. P. Influence of Deposition Temperature on the Structure and Internal Stress of TiN Films Deposited by Filtered Cathodic Vacuum Arc. *J. Vac. Sci. Technol., A* **2002**, *20* (4), 1270−1274.

(59) Xi, Y.; Gao, K.; Pang, X.; Yang, H.; Xiong, X.; Li, H.; Volinsky, A. A. Film Thickness Effect on Texture and Residual Stress Sign Transition in Sputtered TiN Thin Films. *Ceram. Int.* **2017**, *43* (15), 11992−11997.

(60) Daniel, R.; Martinschitz, K. J.; Keckes, J.; Mitterer, C. The Origin of Stresses in Magnetron-Sputtered Thin Films with Zone T Structures. *Acta Mater.* **2010**, *58* (7), 2621−2633.

(61) Thompson, C. V. Grain Growth in Polycrystalline Thin Films. *Interface Sci.* **1998**, *6* (1/2), 85−93.

(62) Pogrebnjak, A. D. Hard and Superhard Nanostructured and Nanocomposite Coatings. In *Nanomaterials-Based Coatings*; Elsevier, 2019; pp 237−337.

(63) Thompson, C. V. Structure Evolution During Processing of Polycrystalline Films. *Annu. Rev. Mater. Sci.* **2000**, *30* (1), 159−190.

(64) Xi, Y.; Bai, Y.; Gao, K.; Pang, X.; Yang, H.; Yan, L.; Volinsky, A. A. Residual Stress and Microstructure Effects on Mechanical, Tribological and Electrical Properties of TiN Coatings on 304 Stainless Steel. *Ceram. Int.* **2018**, *44* (13), 15851−15858.

(65) Pogrebnjak, A. D.; Rogoz, V. M.; Bondar, O. V.; Erdybaeva, N. K.; Plotnikov, S. V. Structure and Physicomechanical Properties of NbN-Based Protective Nanocomposite Coatings: A Review. *Prot. Met. Phys. Chem. Surf.* **2016**, *52* (5), 802−813.

(66) Wen, M.; Hu, C. Q.; Meng, Q. N.; Zhao, Z. D.; An, T.; Su, Y. D.; Yu, W. X.; Zheng, W. T. Effects of Nitrogen Flow Rate on the Preferred Orientation and Phase Transition for Niobium Nitride Films Grown by Direct Current Reactive Magnetron Sputtering. *J. Phys. D: Appl. Phys.* **2009**, *42* (3), No. 035304.

(67) Pogrebnjak, A. D.; Bondar, O. V.; Abadias, G.; Ivashchenko, V.; Sobol, O. V.; Jurga, S.; Coy, E. Structural and Mechanical Properties of NbN and Nb-Si-N Films: Experiment and Molecular Dynamics Simulations. *Ceram. Int.* **2016**, *42* (10), 11743−11756.

(68) Muller, D. A.; Nakagawa, N.; Ohtomo, A.; Grazul, J. L.; Hwang, H. Y. Atomic-Scale Imaging of Nanoengineered Oxygen Vacancy Profiles in SrTiO3. *Nature* **2004**, *430* (7000), 657−661.

(69) Maccagnano-Zacher, S. E.; Mkhoyan, K. A.; Kirkland, E. J.; Silcox, J. Effects of Tilt on High-Resolution ADF-STEM Imaging. *Ultramicroscopy* **2008**, *108* (8), 718−726.

(70) Fitting, H.-J.; Fitting Kourkoutis, L.; Schmidt, B.; Liedke, B.; Ivanova, E. V.; Zamoryanskaya, M. V.; Pustovarov, V. A.; Zatsepin, A. F. Electron Microscopic Imaging of an Ion Beam Mixed SiO_2/Si Interface Correlated with Photo- and Cathodoluminescence. *Phys. Status Solidi A* **2012**, *209* (6), 1101−1108.

(71) Guzman, R.; Gazquez, J.; Mundet, B.; Coll, M.; Obradors, X.; Puig, T. Probing Localized Strain in Solution-Derived YBa2Cu3O7−δ Nanocomposite Thin Films. *Phys. Rev. Mater.* **2017**, *1* (2), No. 024801.

(72) Oveisi, E.; Spadaro, M. C.; Rotunno, E.; Grillo, V.; Hébert, C. Insights into Image Contrast from Dislocations in ADF-STEM. *Ultramicroscopy* **2019**, *200*, 139−148.

(73) Rafaja, D.; Poklad, A.; Klemm, V.; Schreiber, G.; Heger, D.; Šíma, M.; Dopita, M. Some Consequences of the Partial Crystallographic Coherence between Nanocrystalline Domains in Ti−Al−N and Ti−Al−Si−N Coatings. *Thin Solid Films* **2006**, *514* (1−2), 240−249.

(74) Herrera-Jimenez, E. J.; Raveh, A.; Schmitt, T.; Bousser, E.; Klemberg-Sapieha, J. E.; Martinu, L. Solid Solution Hardening in Nanolaminate ZrN-TiN Coatings with Enhanced Wear Resistance. *Thin Solid Films* **2019**, *688*, No. 137431.

(75) Leyland, A.; Matthews, A. On the Significance of the H/E Ratio in Wear Control: A Nanocomposite Coating Approach to Optimised Tribological Behaviour. *Wear* **2000**, *246* (1−2), 1−11.

(76) Ni, W.; Cheng, Y.-T.; Lukitsch, M. J.; Weiner, A. M.; Lev, L. C.; Grummon, D. S. Effects of the Ratio of Hardness to Young's Modulus on the Friction and Wear Behavior of Bilayer Coatings. *Appl. Phys. Lett.* **2004**, *85* (18), 4028−4030.

(77) Caliskan, H.; Panjan, P.; Kurbanoglu, C. Hard Coatings on Cutting Tools and Surface Finish. In *Comprehensive Materials Finishing*; Elsevier, 2017; pp 230−242.

(78) Rafaja, D.; Wüstefeld, C.; Baehtz, C.; Klemm, V.; Dopita, M.; Motylenko, M.; Michotte, C.; Kathrein, M. Effect of Internal Interfaces on Hardness and Thermal Stability of Nanocrystalline Ti0.5Al0.5N Coatings. *Metall. Mater. Trans. A* **2011**, *42* (3), 559−569.

(79) Musil, J. Hard Nanocomposite Coatings: Thermal Stability, Oxidation Resistance and Toughness. *Surf. Coat. Technol.* **2012**, *207*, 50−65.

(80) Babu, K. R.; Guo, G.-Y. Electron-Phonon Coupling, Superconductivity, and Nontrivial Band Topology in NbN Polytypes. *Phys. Rev. B* **2019**, *99*, No. 104508.

(81) Zou, Y.; Wang, X.; Chen, T.; Li, X.; Qi, X.; Welch, D.; Zhu, P.; Liu, B.; Cui, T.; Li, B. Hexagonal-Structured ε-NbN: Ultra-Incompressibility, High Shear Rigidity and a Possible Hard Superconducting Material. *Sci. Rep.* **2015**, *5* (1), No. 10811.

(82) Warcholinski, B.; Gilewicz, A.; Tarnowska, M. The Surface Assessment and the Properties of Selected Multilayer Coatings. *Lubricants* **2023**, *11* (9), 371.

(83) Zhang, Z.; Rapaud, O.; Allain, N.; Mercs, D.; Baraket, M.; Dong, C.; Coddet, C. Characterizations of Magnetron Sputtered CrSiN/ZrN Multilayer Coatings-from Structure to Tribological Behaviors. *Adv. Eng. Mater.* **2009**, *11* (8), 667−673.

(84) Ke, L.; Tao, S.; Fangfang, G.; Feng, H.; Qing, F. Structure and Tribological Behavior of WSiN Coatings with Low Content of Si. *China Surf. Eng.* **2018**, *31* (5), 108−117.

(85) Holmberg, K.; Matthews, A. *Coatings Tribology: Properties, Mechanisms, Techniques and Applications in Surface Engineering*, 2nd ed.; Elsevier, 2009; Vol. 56.

(86) Fehlner, F. P.; Mott, N. F. Low-Temperature Oxidation. *Oxid. Met.* **1970**, *2* (1), 59−99.

(87) Kato, K. Friction and Wear of Passive Metals and Coatings. In *Tribocorrosion of Passive Metals and Coatings*; Woodhead Publishing, 2011; pp 65−99.

(88) Stachowiak, G. W.; Batchelor, A. W. 13 Corrosive and Oxidative Wear. In *Engineering Tribology*, 3rd ed.; Butterworth-Heinemann, 2005; pp 575−594.

(89) Ju, H. High-Temperature Self-Lubricating Metal Nitride-Based Nanostructure Composite Films. In *Friction, Lubrication and Wear*; IntechOpen, 2019.

(90) Safavi, M. S.; Walsh, F. C.; Visai, L.; Khalil-Allafi, J. Progress in Niobium Oxide-Containing Coatings for Biomedical Applications: A Critical Review. *ACS Omega* **2022**, *7* (11), 9088−9107.

(91) Beake, B. D. The Influence of the H/E Ratio on Wear Resistance of Coating Systems − Insights from Small-Scale Testing. *Surf. Coat. Technol.* **2022**, *442*, No. 128272.

(92) Abdoos, M.; Bose, B.; Rawal, S.; Arif, A. F. M.; Veldhuis, S. C. The Influence of Residual Stress on the Properties and Performance of Thick TiAlN Multilayer Coating during Dry Turning of Compacted Graphite Iron. *Wear* **2020**, *454−455*, No. 203342.

(93) Skordaris, G.; Bouzakis, K. D.; Kotsanis, T.; Charalampous, P.; Bouzakis, E.; Breidenstein, B.; Bergmann, B.; Denkena, B. Effect of PVD Film's Residual Stresses on Their Mechanical Properties, Brittleness, Adhesion and Cutting Performance of Coated Tools. *CIRP J. Manuf. Sci. Technol.* **2017**, *18*, 145−151.

(94) Escobar, C.; Villarreal, M.; et al. Tribological and Wear Behavior of HfN/VN Nanomultilayer Coated Cutting Tools. *Ing. Invest.* **2014**, *34* (1), 22−28.

(95) Stachowiak, G. W.; Batchelor, A. W. 14 Fatigue Wear. In *Engineering Tribology*, 3rd ed.; Elsevier, 2005; pp 595−620.

(96) Aksoy, M.; Yilmaz, O.; Korkut, M. H. The Effect of Strong Carbide-Forming Elements on the Adhesive Wear Resistance of Ferritic Stainless Steel. *Wear* **2001**, *249* (8), 639−646.

(97) Pardanaud, C.; Dellasega, D.; Passoni, M.; Martin, C.; Roubin, P.; Addab, Y.; Arnas, C.; Couëdel, L.; Minissale, M.; Salomon, E.; Giacometti, G.; Merlen, A.; Bernard, E.; Mateus, R.; Alves, E.; Siketic, Z.; Radovic, I. B.; Hakola, A. Post-Mortem Analysis of Tungsten Plasma Facing Components in Tokamaks: Raman Microscopy Measurements on Compact, Porous Oxide and Nitride Films and Nanoparticles. *Nucl. Fusion* **2020**, *60* (8), No. 086004.

(98) Addonizio, M. L.; Castaldo, A.; Antonaia, A.; Gambale, E.; Iemmo, L. Influence of Process Parameters on Properties of Reactively Sputtered Tungsten Nitride Thin Films. *J. Vac. Sci. Technol., A* **2012**, *30* (3), No. 031506.

(99) Mercier, F.; Coindeau, S.; Lay, S.; Crisci, A.; Benz, M.; Encinas, T.; Boichot, R.; Mantoux, A.; Jimenez, C.; Weiss, F.; Blanquet, E. Niobium Nitride Thin Films Deposited by High Temperature Chemical Vapor Deposition. *Surf. Coat. Technol.* **2014**, *260*, 126−132.

(100) Chen, X.-J.; Struzhkin, V.; Kung, S.; Mao, H.; Hemley, R.; Christensen, A. Pressure-Induced Phonon Frequency Shifts in Transition-Metal Nitrides. *Phys. Rev. B* **2004**, *70* (1), No. 014501.

(101) Kaiser, R.; Spengler, W.; Schicktanz, S.; Politis, C. Raman Spectra and Superconductivity of Various Phases of a High- T_c Superconductor: NbN. *Phys. Status Solidi* **1978**, *87* (2), 565−573.

(102) Constable, C. P.; Yarwood, J.; Hovsepian, P.; Donohue, L. A.; Lewis, D. B.; Münz, W.-D. Structural Determination of Wear Debris Generated from Sliding Wear Tests on Ceramic Coatings Using Raman Microscopy. *J. Vac. Sci. Technol., A* **2000**, *18* (4), 1681−1689.

(103) Pagnier, T.; Boulova, M.; Sergent, N.; Bouvier, P.; Lucazeau, G. Nanopowders and Nanostructured Oxides: Phase Transitions and Surface Reactivity. *J. Raman Spectrosc.* **2007**, *38* (6), 756−761.

(104) Landon, J.; Demeter, E.; İnoğlu, N.; Keturakis, C.; Wachs, I. E.; Vasić, R.; Frenkel, A. I.; Kitchin, J. R. Spectroscopic Characterization of Mixed Fe−Ni Oxide Electrocatalysts for the Oxygen Evolution Reaction in Alkaline Electrolytes. *ACS Catal.* **2012**, *2* (8), 1793−1801.

(105) Kumar, P.; No-Lee, H.; Kumar, R. Synthesis of Phase Pure Iron Oxide Polymorphs Thin Films and Their Enhanced Magnetic Properties. *J. Mater. Sci.: Mater. Electron* **2014**, *25* (10), 4553−4561.

(106) Zhou, A.; Prakash, J.; Rohde, G. T.; Klein, J. E. M. N.; Kleespies, S. T.; Draksharapu, A.; Fan, R.; Guo, Y.; Cramer, C. J.; Que, L. The Two Faces of Tetramethylcyclam in Iron Chemistry: Distinct Fe−O−M Complexes Derived from [Fe^{IV} (O $_{anti/syn}$)-(TMC)] $^{2+}$ Isomers. *Inorg. Chem.* **2017**, *56* (1), 518−527.

(107) Zhang, Z.; Guan, D.; Gao, G.; Wu, G.; Wang, H. Gasochromic Properties of Novel Tungsten Oxide Thin Films Compounded with

Methyltrimethoxysilane (MTMS). *RSC Adv.* **2017**, *7* (65), 41289–41296.

(108) Jehng, J. M.; Wachs, I. E. Structural Chemistry and Raman Spectra of Niobium Oxides. *Chem. Mater.* **1991**, *3* (1), 100–107.